

AD-772 234

AN EXPERIMENT ON THE WAKE OF A SLENDER  
PROPELLER--DRIVEN BODY

R. L. Gran

TRW Systems Group

Prepared for:

Office of Naval Research  
Advanced Research Projects Agency

June 1973

DISTRIBUTED BY:

**NTIS**

National Technical Information Service  
U. S. DEPARTMENT OF COMMERCE  
5285 Port Royal Road, Springfield Va. 22151

AD 772 234

20086-6006-RU-00

WAKE MIXING STUDIES

15 August 1971 - 30 June 1973

Final Report

AN EXPERIMENT ON THE WAKE OF A  
SLENDER PROPELLER-DRIVEN BODY

R. L. Gran

1973 June

Sponsored by

Advanced Research Projects Agency  
ARPA Order No. 1910  
Program Code No. 3E20

Monitored by

Office of Naval Research  
Arlington, Virginia  
Contract N00014-72-C-0074

DDC  
JAN 21 1974  
B

The views and conclusions contained in this document are those of the author and should not be interpreted as necessarily representing the official policies, either expressed or implied, of the Advanced Research Projects Agency or the U. S. Government.

DISTRIBUTION STATEMENT A
Approved for public release;
Distribution Unlimited

**TRW**  
SYSTEMS GROUP

ONE SPACE PARK REDONDO BEACH CALIFORNIA 90278

UNCLASSIFIED

Security Classification

DOCUMENT CONTROL DATA - R&D		
<small>(Security classification of title, body of abstract and indexing annotation must be entered when the overall report is classified)</small>		
1. ORIGINATING ACTIVITY (Corporate author)		2. REPORT SECURITY CLASSIFICATION
TRW Systems Group		Unclassified
3. REPORT TITLE		
WAKE MIXING STUDIES -- Final Report on AN EXPERIMENT ON THE WAKE OF A SLENDER PROPELLER-DRIVEN BODY		
4. DESCRIPTIVE NOTES (Type of report and inclusive dates)		
Final Report		
5. AUTHOR(S) (Last name, first name, initial)		
Gran, R. L		
6. REPORT DATE	7a. TOTAL NO OF PAGES	7b. NO OF REFS
1973 June	50	16
8a. CONTRACT OR GRANT NO	8b. ORIGINATOR'S REPORT NUMBER(S)	
NO0014-72-C-0074	20086-6006-RU-00	
ARPA Order No. 1910	8c. OTHER REPORT NO'S: (Any other numbers that may be assigned this report)	
Program Code No. 3E20		
10. AVAILABILITY LIMITATION NOTICES		
11. SUPPLEMENTARY NOTES		12. SPONSORING MILITARY ACTIVITY
		Office of Naval Research Arlington, Virginia 22217
13. ABSTRACT The momentumless wake of a slender propeller-driven model in a wind tunnel at a Reynolds number of $6.3 \times 10^4$ (based upon diameter) is examined using the hot-wire anemometer. Measurements of the mean flow field including swirl are presented, as well as measurements of the turbulent intensity and Reynolds stress within the first 20 diameters behind the model. The data are compared with a previous experiment at a similar Reynolds number but which used a blunt body and a high-speed jet as a propulsion source. Significant differences are noted in the development of the two wakes which are caused by body bluntness and propeller-induced swirl. For example, the turbulent intensity is lower by a factor of two for the present data and the wake width is somewhat narrower. The effects of swirl on the mean flow field are important for $x/D \leq 6$ , whereas farther downstream the swirl component primarily affects the turbulent energy balance. A theoretical model of the flow is also presented which describes the flow quite well, given the measured conditions at one location. The constants of the turbulence model are determined experimentally and compared with determinations made for other flow fields. The present values of these constants are comparable, although the strict universality of these constants is not conclusive.		

DD FORM 1473

UNCLASSIFIED

Security Classification

ia

UNCLASSIFIED

Security Classification

14 KEY WORDS	LINK A		LINK B		LINK C	
	ROLE	WT	ROLE	WT	ROLE	WT
Turbulent wake Momentumless wake Low-speed wind tunnel Naudascher experiment Swirl velocity Reynolds stress						

**INSTRUCTIONS**

1. **ORIGINATING ACTIVITY** Enter the name and address of the contractor, subcontractor, grantee, Department of Defense activity or other organization (corporate author) issuing the report.

2a. **REPORT SECURITY CLASSIFICATION** Enter the overall security classification of the report. Indicate whether "Restricted Data" is included. Marking is to be in accordance with appropriate security regulations.

2b. **GROUP** Automatic downgrading is specified in DoD Directive 5200.10 and Armed Forces Industrial Manual. Enter the group number. Also, when applicable, show that optional markings have been used for Group 3 and Group 4 as authorized.

3. **REPORT TITLE** Enter the complete report title in all capital letters. Titles in all cases should be unclassified. If a meaningful title cannot be selected without classification, show title classification in all capitals in parentheses immediately following the title.

4. **DESCRIPTIVE NOTES** If appropriate, enter the type of report, e.g., interim, progress, summary, annual, or final. Give the inclusive dates when a specific reporting period is covered.

5. **AUTHOR(S)** Enter the name(s) of author(s) as shown on or in the report. Enter last name, first name, middle initial. If military, show rank and branch of service. The name of the principal author is an absolute minimum requirement.

6. **REPORT DATE** Enter the date of the report as day, month, year, or month, year. If more than one date appears on the report, use date of publication.

7a. **TOTAL NUMBER OF PAGES** The total page count should follow normal pagination procedures, i.e., enter the number of pages containing information.

7b. **NUMBER OF REFERENCES** Enter the total number of references cited in the report.

8a. **CONTRACT OR GRANT NUMBER** If appropriate, enter the applicable number of the contract or grant under which the report was written.

8b, 8c, & 8d. **PROJECT NUMBER** Enter the appropriate military department identification, such as project number, subproject number, system numbers, task number, etc.

9a. **ORIGINATOR'S REPORT NUMBER(S)** Enter the official report number by which the document will be identified and controlled by the originating activity. This number must be unique to this report.

9b. **OTHER REPORT NUMBER(S)** If the report has been assigned any other report numbers (either by the originator or by the sponsor), also enter this number(s).

10. **AVAILABILITY/LIMITATION NOTICES** Enter any limitations on further dissemination of the report, other than those imposed by security classification, using standard statements such as:

- (1) "Qualified requesters may obtain copies of this report from DDC."
- (2) "Foreign announcement and dissemination of this report by DDC is not authorized."
- (3) "U. S. Government agencies may obtain copies of this report directly from DDC. Other qualified DDC users shall request through \_\_\_\_\_."
- (4) "U. S. military agencies may obtain copies of this report directly from DDC. Other qualified users shall request through \_\_\_\_\_."
- (5) "All distribution of this report is controlled. Qualified DDC users shall request through \_\_\_\_\_."

If the report has been furnished to the Office of Technical Services, Department of Commerce, for sale to the public, indicate this fact and enter the price, if known.

11. **SUPPLEMENTARY NOTES** Use for additional explanatory notes.

12. **SPONSORING MILITARY ACTIVITY** Enter the name of the departmental project office or laboratory sponsoring (paying for) the research and development. Include address.

13. **ABSTRACT** Enter an abstract giving a brief and factual summary of the document indicative of the report, even though it may also appear elsewhere in the body of the technical report. If additional space is required, a continuation sheet shall be attached.

It is highly desirable that the abstract of classified reports be unclassified. Each paragraph of the abstract shall end with an indication of the military security classification of the information in the paragraph, represented as (TS), (S), (C), or (R).

There is no limitation on the length of the abstract. However, the suggested length is from 150 to 225 words.

14. **KEY WORDS** Key words are technically meaningful terms or short phrases that characterize a report and may be used as index entries for cataloging the report. Key words must be selected so that no security classification is required. Identifiers, such as equipment model designation, trade name, military project code name, geographic location, may be used as key words but will be followed by an indication of technical context. The assignment of links, rules, and weights is optional.

UNCLASSIFIED


Security Classification

Prepared for:

OFFICE OF NAVAL RESEARCH  
Arlington, Virginia 22217

Scientific Officer:  
Ralph D. Cooper  
Program Director Fluid Dynamics

Approved:

  
L. A. Hromas, Manager  
Fluid Mechanics Laboratory

TRW Systems Group  
Redondo Beach, California

## SUMMARY

The momentumless wake of a slender propeller-driven model in a wind tunnel at a Reynolds number of  $6.3 \times 10^4$  (based upon diameter) is examined using the hot-wire anemometer. Measurements of the mean flow field including swirl are presented, as well as measurements of the turbulent intensity and Reynolds stress within the first 20 diameters behind the model. The data are compared with a previous experiment at a similar Reynolds number but which used a blunt body and a high-speed jet as a propulsion source. Significant differences are noted in the development of the two wakes which are caused by body bluntness and propeller-induced swirl. For example, the turbulent intensity is lower by a factor of two for the present data and the wake width is somewhat narrower. The effects of swirl on the mean flow field are important for  $x/D \leq 6$ , whereas farther downstream the swirl component primarily affects the turbulent energy balance. A theoretical model of the flow is also presented which describes the flow quite well, given the measured conditions at one location. The constants of the turbulence model are determined experimentally and compared with determinations made for other flow fields. The present values of these constants are comparable, although the strict universality of these constants is not conclusive.

## TABLE OF CONTENTS

	<u>Page</u>
1. INTRODUCTION. . . . .	1
2. TEST FACILITY AND APPARATUS . . . . .	4
2.1 Wind Tunnel and Model . . . . .	4
2.2 Instrumentation . . . . .	5
3. RESULTS . . . . .	6
3.1 Theoretical Model . . . . .	6
3.2 Experimental Results. . . . .	8
3.2.1 Non-Axisymmetry of Wake. . . . .	8
3.2.2 Determination of Propeller Speed for Momentumless Wake Conditions . . . . .	9
3.2.3 The Mean Flow Field. . . . .	10
3.2.4 The Turbulent Field of the Wake. . . . .	13
3.3 Determination of Eddy Viscosity . . . . .	15
3.4 Energy Balance in Wake. . . . .	16
4. COMPARISON OF EVALUATED TURBULENT CONSTANTS WITH OTHER EXPERIMENTAL RESULTS. . . . .	18
5. CONCLUSIONS . . . . .	19
6. RECOMMENDATIONS FOR FUTURE WORK . . . . .	20
REFERENCES . . . . .	22



# LIST OF ILLUSTRATIONS

	Page
1. Photograph of Model . . . . .	24
2. Photograph of Wind Tunnel Installation. . . . .	25
3. Example of Observed Wake Asymmetry. . . . .	26
4. Evaluation of Propeller Speed for Thrust-Drag . . . . .	27
5. The Turbulent Wake Radius . . . . .	28
6. Axial Velocity Profiles, $x/D > 6$ . . . . .	29
7. Axial Velocity and Turbulence Profiles for $2 \leq x/D \leq 4$ . . . . .	30
8. The Decay of the Centerline Velocity Excess . . . . .	31
9. Swirl Velocity Radial Profiles. . . . .	32
10. The Decay of the Maximum Swirl Velocity . . . . .	33
11. The Swirl-Induced Radial Pressure Distribution. . . . .	34
12. Profiles of Axial Turbulent Intensity . . . . .	35
13. The Decay of the Turbulent Intensity. . . . .	36
14. Transverse Turbulence Profiles. . . . .	37
15. Reynolds Stress Profiles. . . . .	38
16. Example of Autocorrelation Function of $u'$ . . . . .	39
17. Integral Scale of Turbulence on the Wake Axis . . . . .	40
18. Radial Variation of Eddy Viscosity. . . . .	41
19. Axial Variation of Eddy Viscosity . . . . .	42
20. Energy Flux Measurements in the Momentumless Wake . . . . .	43



# NOMENCLATURE

$A_B$	Cross-sectional area of model, $\pi R_B^2$
$b^*$	Turbulent wake radius
$b$	Normalize wake radius. $b^*/R_B$
$C_1, C_2, C_3$	Constants defined in Equations 1 - 4
$C_D$	Drag coefficient, $\text{drag}/q_\infty A_B$
$C_p$	Pressure coefficient, $(p-p_\infty)/q_\infty$
$C_T$	Torque coefficient, $\text{torque}/q_\infty A_B R_B$
$D$	Maximum diameter of model
$D_p$	Propeller diameter
$e$	Turbulent energy, $\frac{1}{2} (\overline{u'^2} + \overline{v'^2} + \overline{w'^2})$
$ f_0'' $	Curvature of normalized velocity profile on $q$
$J$	Propeller speed parameter, $nD_p/U_\infty$
$K$	Constant defined in Equation 4
$K_\epsilon$	Dissipation constant, $\epsilon\Lambda/e^{3/2}$
$K_\nu$	Eddy viscosity constant, $\nu_T/\sqrt{e} \cdot \Lambda$
$n$	Propeller speed
$p$	Static pressure
$P_p$	Pitot pressure; $p + q$
$q$	Dynamic pressure, $\frac{1}{2} \rho u^2$
$r$	Distance from wake centerline
$R_B$	Maximum radius of model
$Re_D$	Reynolds number, $U_\infty D/\nu$
$Re_\Lambda$	Turbulent Reynolds number $\sqrt{e}\Lambda/\nu$
$R(\tau)$	Autocorrelation function

$U$	Velocity
$u_d, U_d$	Axial velocity difference from $U_\infty$ , maximum value at given station
$v_s, V_s$	Swirl velocity, maximum value at given station
$u', v', w'$	Turbulent velocity in x, y, z directions
$\hat{u}, \hat{v}, \hat{w}$	Normalized RMS turbulent velocities $\sqrt{u'^2}/U_\infty$ , etc.
$\overline{u'v'}, \overline{u'w'}$	Turbulent Reynolds stress
$x, y, z$	Distances measured from propeller plane, x positive downstream. y positive in North direction. z positive in East direction
$\epsilon$	Turbulent dissipation rate
$\eta$	Propeller efficiency
$\Lambda$	Longitudinal integral scale of turbulence
$\lambda$	Longitudinal microscale of turbulence
$\nu$	Kinematic viscosity
$\nu_T$	Eddy viscosity
$\xi$	Normalized axial dimension $x/D$
$\rho$	Fluid density
$\tau$	Time lag for $R(\tau)$
$\tau^*$	Characteristic time of $R(\tau)$ defined in Equation 12
Subscripts	
$o$	Value on centerline of wake
$\infty$	Value in freestream
ref.	Reference or initial condition
$x, y$	Quantity measured in x or y direction
$s$	Swirl

## 1. INTRODUCTION

The turbulent wake created by a self-propelled body, such as an airplane or a submarine, has recently been a subject of intense research because of its relationship to the question of submarine detection. For example, in an ocean thermocline a submarine wake can sufficiently stir the fluid so as to cause a sudden vertical collapse of the wake which, in turn, generates internal gravity waves (Reference 1). Unfortunately, very little is known about the so-called momentumless turbulent wake either experimentally or theoretically, so that calculations of wake-induced phenomena are unreliable.

It is surprising that so little experimental data exist even for the case of a momentumless wake in a uniform fluid. Only two studies treating the self-propelled wake have been published - that by Naudascher (Reference 2) and by Ginevskii, et. al (Reference 3). In each of these experiments the "body" was a circular disk normal to the oncoming fluid and the method of thrust generation was a high-speed axial jet. This configuration does not necessarily provide a good simulation of a full scale flow field principally because the model is not slender or streamlined and also because a high-speed jet is not a common propulsion mechanism.

It is well known that a blunt body can cause large scale fluctuating disturbances to the passing fluid. An example of such a disturbance is the often studied Karman vortex street. Even at high Reynolds numbers where the entire flow surrounding the body is turbulent this vortex street phenomenon can still be observed (Reference 4). The turbulent wake, on the other hand, is composed of smaller scale eddies on the order of a fraction of the wake radius. Thus, for a blunt body, the large scale body-induced disturbances could mask the development of the turbulent wake. A streamlined body, in contrast, creates much less of a gross flow disturbance and the wake develops in a more realistic manner.

The experiments of Naudascher and Ginevskii, moreover, add mass to the flow by virtue of the jet employed in their test configuration. To the external flow field this mass addition is equivalent to the flow past a point source which has a thrust equal to  $\rho U_\infty m$  (where  $m$  is the source strength). The effect of this flow perturbation on either the force balance or the wake development is not known.

A high speed jet supplies more energy to the flow than is necessary even though the resultant thrust is equal to the body drag (i.e., it is less efficient than most other propulsion devices). An estimate of the propulsive efficiency,  $\eta$ , can be estimated from the relation

$$\eta = \frac{1}{1 + \frac{1}{2} \frac{\Delta V}{U_\infty}}$$

where  $\Delta V$  is the change in fluid velocity imparted by the propulsion device. The excess energy is eventually converted to turbulence in regions of high shear. Thus, it might be expected that the turbulent intensities will be lower for, say, a propeller-driven body than for a jet-driven body.

The use of a propeller as a propulsive mechanism is commonplace for ocean vessels because of its relatively high efficiency. An additional complication, is that a propeller does induce a swirl component within the wake which can have a pronounced effect on its development such as its growth and the decay of the turbulent intensities.

Because of the deficiencies noted in the previous experiments and because of the paucity of experimental data, it was felt that a more realistically created momentumless wake should be experimentally studied. This report describes the results of such an experimental program.

The results of the present experiment on the wake of a slender propeller-driven body are presented in Section 3. These results are compared with previous data in an effort to assess the differences between the two sets of data and to determine if these differences are caused by body shape or propeller-induced swirl.

A set of turbulent model equations are also solved to describe the flow using the measured initial conditions at one station in the wake. This theory is given in Section 3.1 and the result compared with the data in subsequent sections. A comparison of the universality of the three constants obtained from this experiment is made with other free turbulent flows in Section 4.

## 2. TEST FACILITY AND APPARATUS

### 2.1 WIND TUNNEL AND MODEL

This experiment was performed in the TRW low-speed wind tunnel at a freestream velocity of 64 ft/sec. This facility has a test section nominally 11 inches square by 88 inches in length. The cross-sectional area of the tunnel does increase in the flow direction to compensate for wall boundary layer growth and result in constant freestream velocity. The resultant freestream velocity was uniform to within 1% and the turbulence level was measured to be roughly 0.25%.

The model, shown in Figure 1, is a 2.00 inch maximum diameter Rankine ovoid with a 12.5 degree conical boat-tail and with an overall length of 22 inches. A three-bladed propeller, also shown in Figure 1, was used to provide the thrust and is constructed from brass with a diameter of 1.05 inches. The pitch-to-diameter ratio of the propeller blades varies from about 0.95 at the hub to 1.5 at the blade tip and the blades themselves are 0.03 inches thick and have a total area of 33% of the propeller disk area. The propeller was driven by a high-speed air turbine capable of speeds up to 100,000 RPM.

The model was suspended by means of a ball joint at the end of a 0.75 inch O.D. pipe which extends through the convergent section of the wind tunnel. This pipe also serves as the supply and exhaust lines for the turbine air supply. Four small wires (0.014 inch diameter) were used to position and stiffen the pipe against vibrations and were located at the test section entrance. A photograph of the wind tunnel installation is shown in Figure 2. Here, the flow is vertically downward with the compass orientation noted in the figure. For future reference the origin of the coordinate system is located at the plane of the propeller with x measured downstream, y in the northerly direction and z in the easterly direction.

The Reynolds number based on the freestream conditions and the model diameter is  $6.3 \times 10^4$  for the present experiment. This is some 25% greater than the Reynolds number of the Naudascher experiment.

## 2.2 INSTRUMENTATION

Turbulence measurements and mean flow data were obtained using a ThermoSystems constant temperature anemometer (Model 1051). The sensors were single and crossed-wire probes made of 0.00015 inch diameter tungsten wire with a length of 0.050 inches. All wires had a cold resistance of 5-7 ohms and were operated at resistance 50% greater than the cold value.

The output of the anemometer was not linearized because of the low fluctuation levels ( $\sim 10\%$ ). Analytic corrections were made for the mean flow measurements using an in-place wire calibration and King's law - both of which were verified by static and dynamic calibration in an open jet.

Auxiliary equipment used with the anemometer included a Dymec Integrating digital voltmeter (1 second averaging time) (Model 2401B), a Ballantine True RMS meter (Model 320A), a ThermoSystems Correlator (Model 1015C), a ThermoSystems RMS meter (Model 1060), and a Saicor Correlation and Probability Analyzer (Model SAI-42A).

In addition to the anemometer data, mean flow information was also obtained using a Pitot tube in conjunction with Pace differential pressure transducer (Model P90D) and a Whittaker Carrier Demodulator (Model CD10). The demodulator output was monitored on the abovementioned digital voltmeter. The propeller speed was measured using a General Radio Corp. Strobotac (Type 1531-A).



### 3. RESULTS

#### 3.1 THEORETICAL MODEL

One important result of the present investigation is the concurrence of the present data with one currently popular turbulence model. This model, which is a simplified version of that proposed by Ng and Spaulding (Reference 5), assumes that the shear stress can be computed from an "eddy viscosity"\* such that  $\nu_T \sim \sqrt{e} \cdot \Lambda$  (originally attributed to Prandtl and Kolmogorov) and that the rate of dissipation of turbulent energy is  $\epsilon \sim e^{3/2}/\Lambda$  where  $e$  is the local turbulent energy ( $= \frac{1}{2} \overline{u_i'^2}$ ) and  $\Lambda$  is the longitudinal integral scale of the turbulence.\*\* The simplification introduced here is that the integral scale  $\Lambda$  is a fixed fraction of the width of the turbulent region. Given these relations along with the experimental observation that  $\nu_T \approx \nu_T(x)$  only, relatively simple differential equations for the growth rate of the wake, the decay of the mean field and the decay of the turbulent energy can be derived.

Without going into detail these are:

(Integrated  $r^2 \cdot$  Momentum Equation)

$$b^4 U_D = \text{constant} \quad (1)$$

( $\epsilon$  Momentum Equation)

$$\frac{1}{U_D} \frac{dU_D}{d\xi} = -4C_1 e_0^{1/2}/b \quad (2)$$

\* The author is aware of the limitations of such a concept for certain flows such as the wall jet.

\*\* This is strictly valid only for large turbulence Reynolds number

$R_\Lambda = \frac{\sqrt{e}\Lambda}{\nu}$ . For the present tests  $R_\Lambda \gtrsim 300$  which is sufficient to justify the use of the stated dissipation law.

(Conservation of Angular Momentum)

$$b^3 V_s = \text{constant} \quad (3)$$

(Integrated Turbulent Energy Equation)

$$\frac{d}{d\xi} (e_0 b^2) = 2C_2 e_0^{3/2} b + C_3 \frac{dV_s^2 b^2}{d\xi} \quad (4)$$

where

$$C_1 \equiv K_v |f_0''| (\Lambda_0/b)$$

$$C_2 \equiv K \cdot K_e / \Lambda_0 / b$$

$$K_v \equiv \nu_t / \sqrt{e} \cdot \Lambda$$

$$K_e \equiv \epsilon \cdot \Lambda_0 / e_0^{3/2}$$

$K$  = constant from averaging

$e$  and  $\epsilon$  over the entire wake ( $\approx 0.77$ ),  $C_3$  = constant from relating the angular momentum integral to the maximum swirl velocity  $V_s$  and  $|f_0''|$  is the curvature of the axial velocity profile on the wake axis. In the derivation of these equations the effect of swirl on the mean flow field is neglected as is the production of turbulence from the mean axial flow field — both of which decay like  $\xi^{-1/2}$  relative to the retained terms.

As a further simplification, the turbulence production term  $C_3 d(V_s^2 b^2)/d\xi$  is taken proportional to  $e_0^{3/2} b$  so that the turbulent energy equation may be written

$$\frac{d}{d\xi} (e_0 b^2) \approx -2C_2^* e_0^{3/2} b \quad (5)$$

Equations (1), (2), (3) and (5) can then be integrated in closed form to give:

$$b/b_{\text{REF}} = \left[ (1 + (2C_1 + C_2^*)) \frac{\sqrt{e_{\text{REF}}}}{b_{\text{REF}}} (\xi - \xi_{\text{REF}}) \right]^{\frac{C_1/C_2^*}{2C_1/C_2^* + 1}}$$

$$\begin{aligned}
U_0/U_{REF} &= [(1 + (2C_1 + C_2^*)) \frac{\sqrt{e_{REF}}}{b_{REF}} (\xi - \xi_{REF})]^{-\frac{4C_1/C_2^*}{-2C_1/C_2^* + 1}} \\
C_0/C_{0REF} &= [(1 + (2C_1 + C_2^*)) \frac{\sqrt{e_{REF}}}{b_{REF}} (\xi - \xi_{REF})]^{-\frac{2C_1/C_2^* + 2}{-2C_1/C_2^* + 1}} \\
V_s/V_{sREF} &= [(1 + (2C_1 + C_2^*)) \frac{\sqrt{e_{REF}}}{b_{REF}} (\xi - \xi_{REF})]^{-\frac{3C_1/C_2^*}{-2C_1/C_2^* + 1}}
\end{aligned} \tag{6}$$

Using the measured values of  $K_v = 0.4$ ,  $K_e = 0.53$ ,  $\Lambda_0/b = 0.21$ ,\* and  $|f_0''| \approx 8.3$  so that  $C_1 = 0.767$ ,  $C_2 = 1.94$  and  $C_2^* = 1.61$  along with the reference conditions taken at  $x/D = 6.0$  from the present experiment gives

$$\begin{aligned}
b(\xi)/b(6) &= [1 + 0.213 (\xi - 6)]^{0.244} \\
U_0(\xi)/U_0(6) &= [1 + 0.213 (\xi - 6)]^{-0.98} \\
\tilde{U}_0(\xi)/\tilde{U}_0(6) &= [1 + 0.213 (\xi - 6)]^{-0.755} \\
V_s(\xi)/V_s(6) &= [1 + 0.213 (\xi - 6)]^{-0.732}
\end{aligned} \tag{7}$$

Plots of these relations are given in Figures 5, 8, 10 and 13 along with the experimental data and the comparison between the two is seen to be excellent over the region surveyed.

## 3.2 EXPERIMENTAL RESULTS

### 3.2.1 Non-Axisymmetry of Wake

Despite considerable effort a perfectly round wake was never achieved during the course of this experiment. An example of the resultant momentumless wake shape is given in Figure 3 where a map of the turbulent energy contours is shown at  $x/D = 15$ . As can be seen, the wake

---

\*The values of these constants computed from other experimentally realized flows is given in Section 4.

is elongated in the NW-SE direction. This same shape was found at all survey stations despite changes in either model position or the model angle-of-attack (by swiveling about the ball joint connection to the pipe).

With the model removed from the test section no appreciable non-uniformity could be detected in the freestream flow which could account for this behavior. Furthermore, attempts to correct the problem such as strut-mounting the model, forcing the flow through a screen at the test section entrance, or lowering the model farther into the test section were all unsuccessful.

The cause for the asymmetry is believed by the author to be a small cross-flow at the bow of the model which is related to the non-symmetric convergent section upstream of the test section.

Mean flow surveys of the wake (both hot-wire and Pitot) show that the model drag (fluid velocity less than freestream) is contained at the two ends of the elongated wake whereas the propeller thrust (fluid velocity greater than freestream) is distributed over the middle of the wake. Wake surveys were generally taken along the two lines indicated in Figure 3 once the center had been found by a preliminary search. Entire maps of the flow were made at several stations to determine the momentum defect and to obtain the turbulent map such as shown in Figure 3.

It should be mentioned that the wake flow was extremely sensitive to the model angle-of-attack. A pitch or yaw angle of 0.2 degrees could easily be observed at  $x/D = 8$  because the propeller jet (or wash) would be off to one side of the body wake. The final model alignment was achieved by repeating surveys at  $x/D = 8$  until the most symmetric wake was found.

### 3.2.2 Determination of Propeller Speed for Momentumless Wake Condition

Pitot pressure maps were obtained at  $x/D = 6$  and  $x/D = 10$  for several propeller speeds in order to determine when the resultant propeller thrust equaled the body drag. Assuming that

$$u_D/U_\infty = \frac{1}{2} (P_p - P_{p\infty})/q_\infty \quad (8)$$

these maps were used to compute the net drag in the wake by manually integrating with a planimeter. The results of these calculations are shown in Figure 4 where the wake drag is normalized by the body drag ( $C_D \approx 0.29$  determined by a similar procedure) and the propeller speed is given in terms of the advance ratio  $J \equiv nD_p/U_\infty$ . All subsequent measurements were made at a propeller speed corresponding to  $J \equiv 1.58 \pm 0.005$ . The actual propeller speed at this condition is around 67,000 RPM which was held constant to within  $\pm 300$  RPM by regulating the turbine air supply and monitoring with the Strobotac. A tribute is due the manufacturer of the air turbine\* in that so high a speed could be easily maintained over the course of the measurements (150 to 200 hours or more). Further, one can imagine the difficulties encountered in balancing the propeller and drive shaft at such high speeds which was accomplished by a trial and error approach.

### 3.2.3 The Mean Flow Field

The measurements of the wake radius obtained from the hot-wire surveys are shown in Figure 5. The wake radius,  $b^*$ , is defined here as the location where the axial turbulent intensity dropped to one-half of the centerline value. Data points are shown for two different probes and the upper set of points represent the x-axis measurement and the lower set the y-axis measurement (see Figure 3 for orientation). An equivalent or mean wake radius defined as

$$b^*/R_B \equiv [b_x^* \cdot b_y^*/R_B^2]^{1/2}$$

is indicated by the solid circles. Shown also is the wake radius measured by Naudascher downstream of a jet-driven circular disk. The present results are somewhat smaller than the disk wake results and appear to reach similarity ( $b^* \approx x^a$ ) sooner. The growth of the present wake is seen to be

---

\*DOTCO, Inc., Hicksville, Ohio

in excellent agreement with the theoretical curve indicated by the heavy dashed line. The growth rate over the region  $6 < x/D < 20$  is approximately  $x^{0.28}$ . Much farther downstream the theory indicates the growth rate will decrease slightly to  $x^{0.244}$ .

The wake velocity profiles  $u_D/U_\infty$  for  $x/D \geq 6$  are shown in Figure 6 for the x-axis surveys. Velocity profiles for  $x/D = 2, 3$  and  $4$  are shown in Figure 7 where the near-field effects of the propeller dominate (such as swirl-induced pressure and propeller thrust distribution). Note that close to the body that the propeller acts like an annular jet and that this near field effect dies out downstream of  $x/D \approx 6$ .

The maximum velocity excess measurements  $U_D/U_\infty$  are shown in Figure 8 where measurements other than those taken from Figure 6 are presented.\* The three determinations of  $U_D/U_\infty$  are quite consistent with one another. Indicated on this figure is the near-field effect which causes the centerline velocity to be less than the peak velocity for  $x/D \lesssim 6$ . The centerline velocity distribution of Naudascher is also shown which is initially much higher than the present experiment [ $U_D(x=0)/U_\infty \approx 3.64$  compared to a value of 1.3 or so here) and exhibits a distinctly different decay rate over the first 20 body diameters. The theoretical prediction of Equation (7) is seen to be in excellent agreement with the data.

Measurements of the swirl velocity (obtained from the crossed-wire anemometer along the z-axis) are shown in Figure 9. Here, an attempt is made to display the similarity of the profiles by normalizing the swirl velocity by the local maximum value and normalizing the radial distance by the turbulent wake radius. The inner 20 percent of the wake is seen to be in solid body rotation ( $v_s \sim r$ ) and the maximum swirl velocity occurs at  $r/b^* \approx 0.25$  to  $0.3$ . The solid line faired through the data has been used to compute the radial swirl-induced pressure distribution, the angular momentum and the flux of swirl energy.

---

\* For the reduction of the Pitot tube data to velocity the local static pressure was computed using the swirl velocity data and the turbulent intensity data. Direct measurement of the static pressure was not made as it was quite small ( $\approx 0.01 q_\infty$ ).

The maximum swirl velocity measurements are shown in Figure 10 along with the theoretical line corresponding to  $V_s b^3 = \text{constant}$  (i.e., conservation of angular momentum). It should be noted that the swirl velocities are comparable in magnitude to the axial flow velocities.

The swirl-induced pressure distribution calculated from

$$p_\infty - p(r) = \rho_\infty \int_r^\infty v_s^2 \frac{dr}{r} \quad (10)$$

and using the faired line from Figure 9 is shown in Figure 11. The radial swirl-induced pressure field is normalized by the axis pressure which is calculated to be  $C_{p0 \text{ swirl}} = -149 (V_s/U_\infty)$  from Equation (10). The swirl induced pressure deficit from freestream is seen from Figure 11 to be significant only in the core of the wake ( $r/b \lesssim 0.5$ ). The turbulence-induced pressure deficit in the wake given by  $C_{p \text{ TURB}} \approx -2 u'^2$  is slightly less on centerline than the swirl-induced pressure deficit.

The torque exerted by the propeller on the fluid has also been calculated and the torque coefficient defined as

$$C_T = \frac{\text{Torque}}{q_\infty A_B \cdot R_B} \quad (11)$$

has a mean value of  $0.075 \pm 0.015$ . Incidentally, the overall efficiency of the propeller defined as the thrust power ( $\text{drag} \cdot U_\infty$ ) divided by total input power to the propeller ( $\text{Torque} \cdot \text{shaft speed}$ ) or  $\eta_{\text{PROP}} = \frac{1}{2\pi} (C_D/C_T \cdot J)$  is 0.41. This is somewhat lower than expected but not unreasonable in light of the large Reynolds number difference [ $0(10^3)$ ] between the model and full scale propellers.

Lastly, the rotation of the wake "core" has been computed by integrating the measured angular swirl velocity along the wake. As the flow proceeds from 3 to 20 diameters behind the body, the inner part of the wake revolves nearly 0.8 revolutions. Closer to the propeller, of course, the swirl is more intense causing perhaps 2 to 6 revolutions by  $x/D = 3$ . This swirling motion could be very important in mixing up a wake inasmuch as this is a gross convective-type motion as opposed to the smaller scale turbulent mixing.



### 3.2.4 The Turbulent Field of the Wake

The axial turbulent intensity ( $\sqrt{u'^2}/U_\infty \equiv \tilde{u}$ ) distributions are shown in Figure 12 where the centerline intensity and the wake radius have been used to normalize the intensity and radial position respectively. The magnitude of the centerline intensity  $\tilde{u}_0$  is shown in Figure 13 where, again, other measurements are also included. Note that the present results are a factor of 2 or so lower than observed by Naudascher for the jet-driven disk wake. This is a consequence of the fact that a large propeller is a more efficient propulsion device than a small high-speed jet. The decay rate of the turbulent intensity is nearly the same for both experiments, however. The theoretical prediction given by Equation (7) is seen to predict the decay rate quite well although it does underestimate the data by 5% or so.

The transverse components of turbulence  $\tilde{v}$  and  $\tilde{w}$  were also measured by means of the crossed wire and a typical profile is shown in Figure 14 taken at  $x/D = 8$  along with a line representing the axial fluctuations,  $\tilde{u}$ . Although there are noticeable differences between  $\tilde{u}$  and  $\tilde{v}$  or  $\tilde{w}$ , the overall impression is that the three intensities are equal over the bulk of the wake. This fact will be used to relate the turbulent energy  $e$  to the axial intensity (i.e.,  $e^{1/2} \approx \sqrt{3/2} \tilde{u}$ ).

Measurements of the Reynolds stress  $\overline{u'v'}$  are shown in Figure 15 for transverses taken along the x-axis. The asymmetry of these profiles corresponds to the observed asymmetry of the mean velocity profiles (Figure 6).

In addition to determining the turbulent intensities and Reynolds stresses the anemometer signal was also connected to the Correlation and Probability analyzer for a more thorough statistical analysis. Auto-correlation functions of the axial turbulence component were taken at a number of stations along the wake axis and also outward along a radius. A typical example of the  $u'$  autocorrelation function  $R(\tau)$  is shown in Figure 16 for  $x/D = 10$ . Note that  $R(\tau)$  is closely represented by  $e^{-\tau/\tau^*}$  and that no periodic behavior is observed.\*

\* At  $x/D = 2$  at the peak axial velocity location a weak periodic signal could be seen in the autocorrelation function corresponding to the propeller frequency (1.1 KHz). By  $x/D = 3$  this behavior could no longer be detected--it presumably being destroyed by the turbulence.

The common definition of the integral scale of turbulence is (accepting Taylor's hypothesis)

$$\Lambda_0 \equiv U \int_0^{\infty} R(\tau) d\tau \quad (12)$$

when  $R(\tau) = e^{-\tau/\tau^*}$  this becomes

$$\Lambda_0/D = \frac{U\tau^*}{D} \quad (13)$$

The measurements of  $\Lambda_0/D$  determined in this manner are shown in Figure 17 for the wake centerline. Shown also are the data of Naudascher for the jet-driven disk which are somewhat greater than found here. The measurements of  $\Lambda$  have also been normalized by the local wake radius and the fact that these two are proportional is shown by the solid line which indicates  $\Lambda_0/b^* \approx 0.21$ . This is still somewhat smaller than found by Naudascher who reports  $\Lambda_0/b^* \approx 0.28$  for  $x/D \lesssim 20$  but decreasing to 0.21 by  $x/D \approx 50$ . The fact that the present experiment shows  $\Lambda/b^* = \text{constant}$  has been used in the theoretical analysis previously given.

Incidentally, the turbulent integral scale size was also measured for the drag wake and a value of  $\Lambda/b^* \approx 0.25 \pm 0.02$  was determined.

Across the momentumless wake the turbulent scale size was observed to increase somewhat toward the edge of the wake. This increase is undoubtedly effected by intermittency (which was not measured) and is consistent with the assumption that  $v_T$  is constant across the wake (e.g., since  $v_T \approx \sqrt{e} \Lambda \approx \sqrt{e_0} \Lambda_0$  then  $\Lambda/\Lambda_0 = [e/e_0]^{-1/2}$ ).

The probability density of axial fluctuations and transverse fluctuations were also measured and found to be very close to a normal distribution--at least on the wake axis. This result was found at all stations even as close as  $x/D = 2$ . Probability density measurements away from the wake axis were skewed which reflects the intermittent nature of the flow near the wake edge.

An attempt was also made to measure the microscale of turbulence by measuring the quantity  $\overline{(\partial u'/\partial t)^2}$  and using the formula given by Hinze (Reference 6)

$$\lambda^2 \approx U^2 \overline{u'^2} / \overline{(\frac{\partial u'}{\partial t})^2} \quad (14)$$

These measurements were, however, not repeatable from day-to-day and moreover appeared somewhat large. This is probably caused by the fact that the length of the wire was the same order as microscale. A wire length correction procedure outlined by Wygnanski and Fiedler (Reference 7) was not used because of the unrepeatability of the  $\lambda$  measurements (30 percent variation).

### 3.3 DETERMINATION OF EDDY VISCOSITY

The mean velocity profiles and the Reynolds stress measurements (Figures 6 and 15, respectively) were used to compute the turbulent or "eddy" viscosity through

$$\nu_T \equiv \frac{\overline{u'_i u'_j}}{\partial u_i / \partial x_j} \quad (15)$$

This procedure is admittedly inaccurate by virtue of the fact that experimental data must be differentiated. Nevertheless, its evaluation was felt important enough to warrant the effort especially in light of the fact that Naudascher's data indicate that the eddy viscosity is roughly constant throughout the wake and which is at odds with recent scaling laws.

The radial variation of the eddy viscosity is shown for one station ( $x/D = 6$ ) in Figure 18 where, except near the edge, it appears to be relatively constant. The axial variation computed for each profile at the point of maximum slope and maximum  $\overline{u'v'}$  for each side of the wake is shown in Figure 20 normalized by the laminar viscosity  $\nu$ . The vertical bars indicate the inaccuracy of the calculation. Note that the turbulent viscosity decreases by a factor of 2 to 2-1/2 over the region  $3 < x/D < 15$ , which is in contrast to the blunt body jet-propelled result. Shown also is the Prandtl-Kolmogorov eddy viscosity relation  $\nu_T = K_\nu \sqrt{\epsilon} \lambda$ . For a value of  $K_\nu \approx 0.4$  this relation provides an excellent approximation to the experimental data.

### 3.4 ENERGY BALANCE IN WAKE

The integrated flux of various forms of energy (turbulent, swirl and mean flow) along the wake have also been computed. These results are shown in Figure 20 where the various fluxes have been normalized by the model drag power ( $\text{drag} \cdot U_\infty$ ). For example, the turbulent energy flux is given by

$$\dot{E}_{\text{turb}} = \int_{\text{wake}} u e \, d\sigma \quad (16)$$

and the integral is evaluated by manual integration of the contour map shown in Figure 3. Similar techniques were used to calculate the swirl energy flux  $\dot{E}_{\text{swirl}} = \int_{\text{wake}} u (v_s^2/2) \, d\sigma$  and mean flow energy flux  $\dot{E}_{\text{mean}} = \int_{\text{wake}} u (u_d^2/2) \, d\sigma$ . Note that the all energy fluxes are quite small compared to the model drag power--less than 10 percent downstream of  $x/D = 4$ . Further, the flux of turbulent energy is far greater than either the swirl energy flux or mean flow energy flux. The decay rates of the turbulent energy flow and the swirl energy flux are comparable whereas the mean flow energy decays somewhat more rapidly which is in agreement with the theoretical model.

Shown for comparative purposes is the amount of turbulent energy deposited into the wake from the boundary layers which was computed using the flat plate data of Klebanoff (Reference 8 and taken from Reference 9) and using Schlichting (Reference 10) to estimate the boundary layer thickness and friction drag. This estimate shows that the bulk of the turbulent energy is generated downstream of the propeller by the axial and swirl velocity gradients rather than simply being convected through the propeller from the boundary layers.

The dissipation rate of turbulent energy can be computed by assuming that the loss of swirl and mean flow energies is effectively a source or production term for the turbulent energy. Assuming that the dissipation rate of turbulent energy on centerline is proportional to  $e_o^{3/2}/\Lambda_o$ , the dissipation constant is found to be  $0.53 \pm 0.02$  which is in fair agreement with the

value determined from other experimental flows--see Section 4 for a more detailed explanation. The effective dissipation constant used in the theoretical model is 0.44 which was calculated from the measured turbulent energy flux curve shown in Figure 21.

#### 4. COMPARISON OF EVALUATED TURBULENT CONSTANTS WITH OTHER EXPERIMENTAL RESULTS

In the formulation of a set of turbulence model equations such as that of Ng and Spaulding, or others, one has the hope that the few arbitrary constants used to characterize the turbulence might be universal in some sense. In other words, these constants should be independent of the particular flow field under investigation. In the present experiment three such constants were evaluated for the case of the momentumless wake with swirl. These are  $K_v$ , the eddy viscosity constant;  $K_\epsilon$ , the dissipation constant; and  $\Lambda_0/b^*$ , the turbulent integral scale size normalized by a characteristic dimension of the extent of turbulent flow, and it is of interest to see how these values compare with other experimentally realized flows.

For this comparison five other flows have been chosen--two planar flows (References 11, 12), two axisymmetric flows (References 7, 13, 14), and homogeneous grid turbulence (References 14, 16)\*. The evaluation of the five turbulent quantities  $e$ ,  $\Lambda$ ,  $v_T$ ,  $\epsilon$  and  $b^*$  have all been evaluated from the data where possible or estimated if necessary. The results of this comparison are shown in Table 1. Also shown in this table is the turbulent Reynolds number  $R_\Lambda$  which should be larger than 30 or so to insure that any laminar phenomena are indeed small compared to the turbulent phenomena.

A cursory examination of Table 1 indicates that complete universality of the three turbulent constants has not been achieved. A factor of 3 or 4 variation in  $K_v$  is noted whereas the variation in  $K_\epsilon$  and  $\Lambda/b^*$  is within a factor of 2. The constants derived from the present experiment look reasonable compared to other flows although  $K_v$  is somewhat higher than average and  $\Lambda/b^*$  is somewhat lower. Whether these small differences are caused by the particular flow field or by experimental inaccuracies is unknown.

---

\*The author would like to acknowledge the assistance of Dr. I. E. Alber of TRW in locating these references and the calculation of the parameters from the unpublished data.

## 5. CONCLUSIONS

Based upon the present experimental results for the wake of a slender propeller-driven body the following conclusions are drawn:

- The wake development is significantly different from previously self-propelled experimental results obtained for a blunt body driven by a high speed jet. For example, in the present experiment the wake is narrower and the turbulent intensities are lower by a factor of two. Further, the integral scale size is 25% lower and the eddy viscosity is observed to decrease with distance aft.
- The effect of propeller swirl on the mean axial flow field is confined to the region  $x/D \lesssim 6$ . Downstream of this, the swirl effects the flow field by acting as a source of turbulent energy. The swirl velocities were observed to be larger than the axial velocity deviations. The "core" of the wake ( $r \lesssim 0.25b$ ) was found to be in solid body rotation.
- From measurements of the eddy viscosity, integral scale size and turbulent dissipation rate a simple turbulence model was found which quite accurately described the wake development using measured initial conditions at  $x/D = 6$ . This turbulence model would predict that far downstream in the wake that the wake radius would increase as  $x^{0.244}$ , the turbulent intensity would decrease as  $x^{-0.755}$  and the axial and swirl velocities would decrease as  $x^{-0.98}$  and  $x^{-0.73}$ , respectively.
- The turbulence constants determined in this experiment compare adequately with determinations made in other flow fields (jets, wakes, and shear layers). While it cannot be said these constants are universal, the variation from flow is tolerable (factor of 2 or 3).



## 6. RECOMMENDATIONS FOR FUTURE WORK

Even with the experimental results presented in this report, the understanding of the development of a full scale momentumless wake is still not complete. For example, the degree of swirl is not simulated exactly here and the effects of stratification or measurements of the turbulent mixing were not treated at all. It is recommended therefore that the following experiments be pursued:

- Examine the effect of different diameter propellers and propellers with differently pitched blades. These two effects directly influence the axial and swirl velocity fields and could, perhaps, substantially change their relative contributions to the decay of the turbulence.
- Measurement of the swirl flow Reynolds stress is also of importance. This effectively gives the rate at which the swirl component is converted to turbulence. Very little is known of how to model this particular Reynolds stress and its determination could impact other fields such as aircraft wake vortices or swirling jets.
- The initial degree-of-mixing in the wake could be determined by creating a gradient of a passive scalar in the tunnel freestream. Measurement of the gradient within the wake is a direct measure of how well mixed the wake flow is. This would have direct impact on calculations which account for the gravitational restoring forces for flows within a stratified fluid.

TABLE 1  
TURBULENT MODEL CONSTANTS

	Grid Turb. (Ref. 15)	2-D Shear Layer (Ref. 11)	2-D Jet (Ref. 12)	Axisym Wake (Ref. 13) <del>Axis-Wake</del> Supersonic (Ref. 14)	Axisym Jet (Ref. 7)	Self Propelled Wake (Present Results)
Turbulent Reynolds Number $R_A \equiv \frac{\sqrt{\epsilon} \Lambda}{\nu}$	$\infty$	9000	3000 to 12,000	$\frac{1700}{350}$	8600	400
Eddy Viscosity Constant $K_\nu \equiv \frac{\nu_T}{\sqrt{\epsilon} \Lambda}$	-	0.11	0.13 to 0.3	$\frac{0.33}{0.15}$	0.16	0.4
Dissipation Constant $K_\epsilon \equiv \frac{\epsilon \Lambda}{e^{3/2}}$	0.4	0.38	0.4 to 1.0	-	0.26 to 0.65	0.53
Turbulent Scale Size $\Lambda_0/b^*$	-	0.43	0.3 to C.7	$\frac{0.25}{(assumed)} \frac{1}{0.38}$	0.27	0.21

## REFERENCES

1. Ko, D. R. S., "Collapse of a Turbulent Wake in a Stratified Medium," Fleet Vulnerability Studies Final Report, Vol. II, TRW Report 18202-6001-R0-00, November 1971.
2. Naudascher, E., "Flow in the Wake of a Self-Propelled Bodies and Related Sources of Turbulence," J. Fluid Mech. 22, part 4, pp. 625-656 (1956).
3. Ginevskii, A. S., Pochkina, K. A. and Ukhanova, L. N., "Propagation of Turbulent Jet Flow with Zero Excess Momentum," Fluid Dynamics Academy of Sciences USSR, Vol. 1, No. 6, November-December 1966, Faraday Press, Inc.
4. Roshko, A., Private Communication.
5. Ng, K. H. and Spaulding, D. B., "Turbulence Model for Boundary Layers Near Walls," Physics of Fluids, Vol. 13, No. 1, January 1972.
6. Hinze, J. O., Turbulence - An Introduction to Its Mechanism and Theory, McGraw-Hill Book Company, 1959.
7. Wygnanski, I. and Fiedler, H., "Some Measurements in the Self-preserving Jet," J. Fluid Mech. 38, part 3, pp. 577-612, 1970.
8. Klebanoff, P. S., NACA Report 1247, 1955.
9. Kistler, A. L., "Fluctuation Measurements in a Supersonic Turbulent Boundary Layer," Physics of Fluids, Vol. 2, No. 3, 1959.
10. Schlichting, H., Boundary Layer Theory, 4th Ed.
11. Wygnanski, I. and Fiedler, H., "The Two-dimensional Mixing Region," J. Fluid Mech. 41, part 2, pp. 327-361, 1970.
12. Bradbury, L. J. S., "The Structure of a Self-preserving Turbulent Plane Jet," J. Fluid Mech. 23, part 1, pp. 31-64, 1965.
13. Chevray, R., "The Turbulent Wake of a Body of Revolution," Trans. ASME, Series D - Journal of Basic Engineering, Vol. 90, pp. 275-284, 1968.
14. Demetriades, A., "Turbulent Measurements in an Axisymmetric Compressible Wake," Phys. of Fluids 11, No. 9, September 1968.

15. Finson, M. L., "Hypersonic Wake Aerodynamics at High Reynolds Numbers," AIAA Paper 72-701, presented at AIAA 5th Fluid Plasma Dynamics Conference, Boston, Massachusetts, June 26-28, 1972.
16. Trousov, B.G., "The Establishment of a Relationship between the Intensity Value and the Dissipation of Energy of Turbulence," Fluid Mechanics-Soviet Research, Vol. 1, No. 5, 1972.

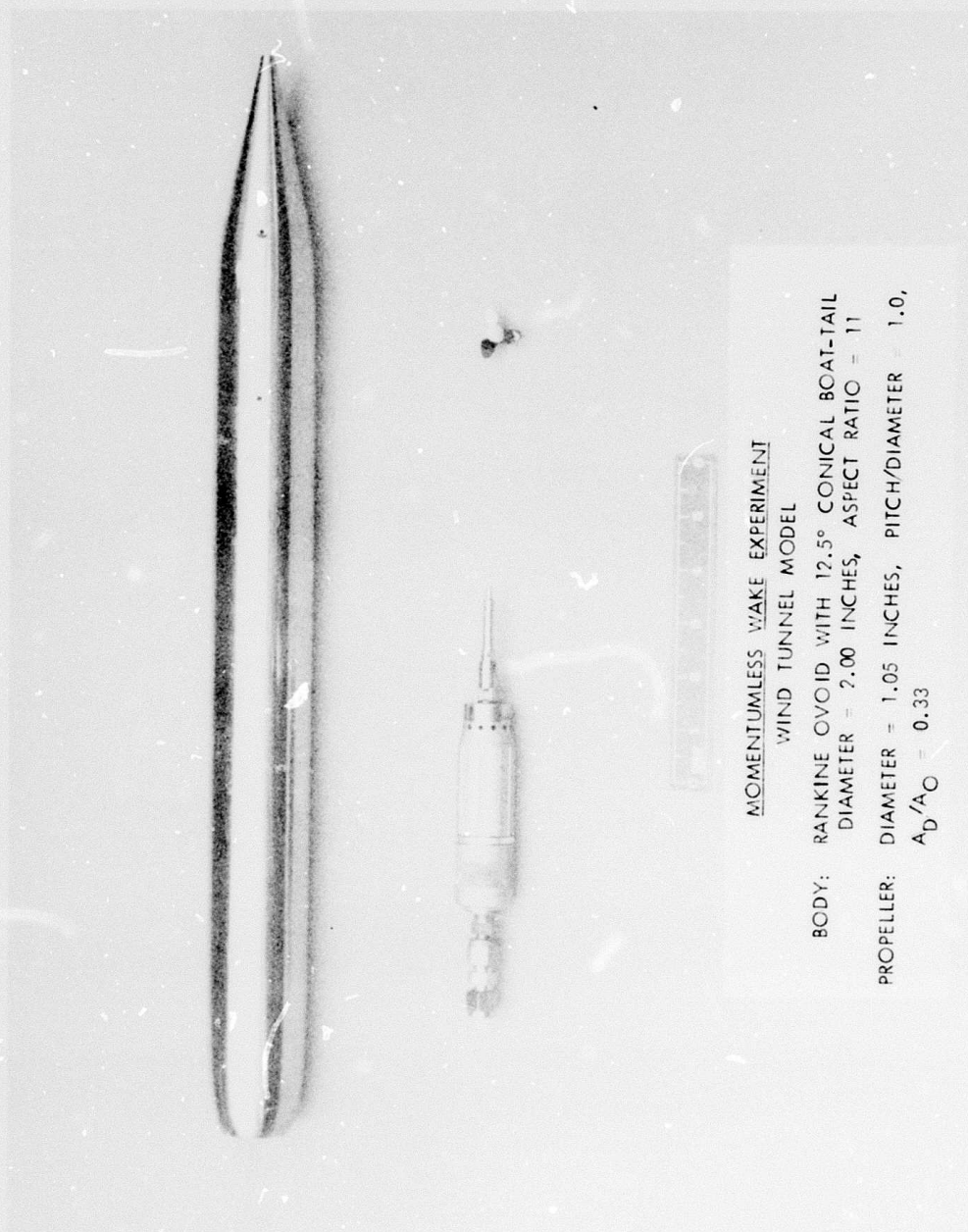
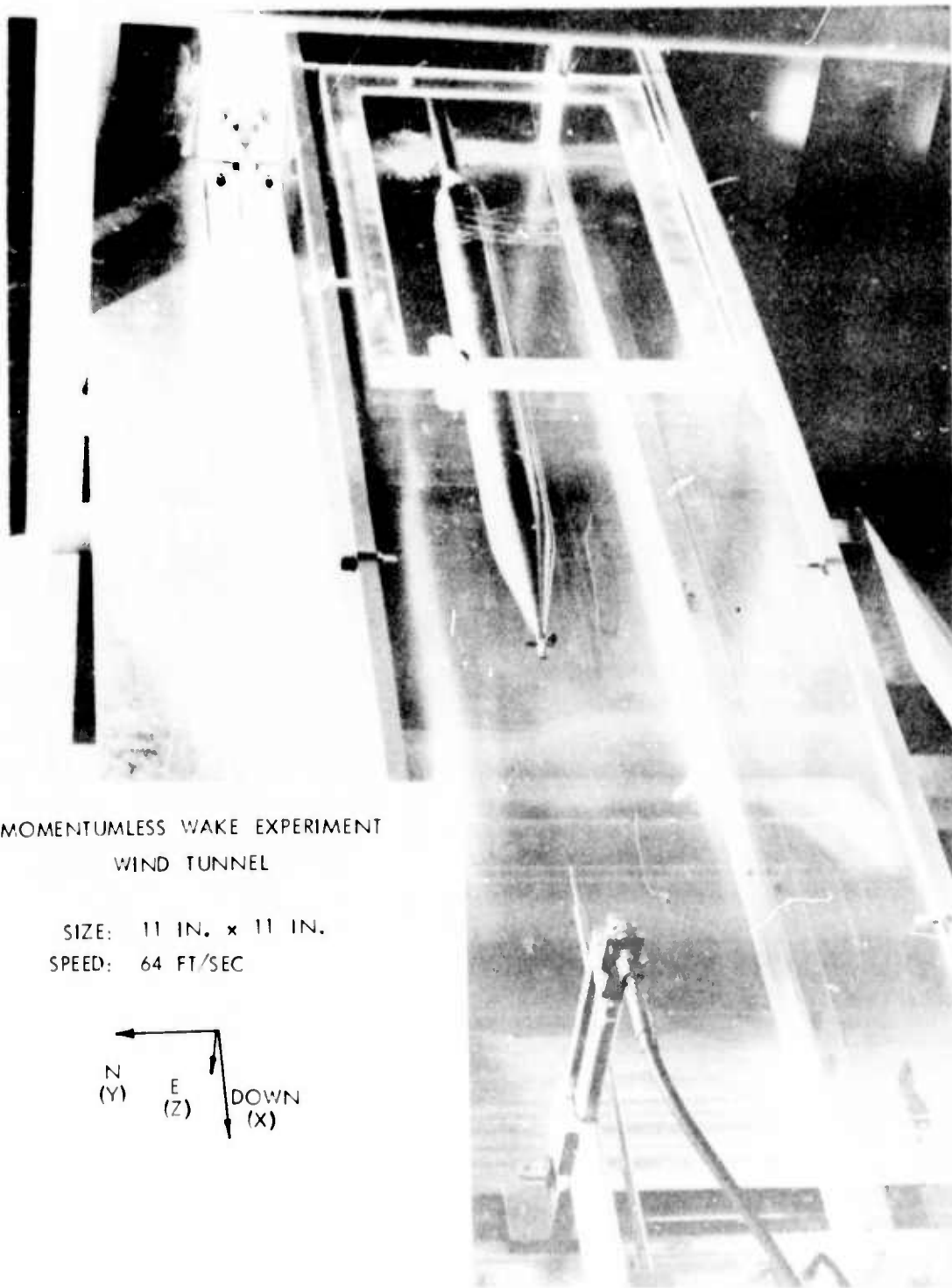


Figure 1. Photograph of Model 1



MOMENTUMLESS WAKE EXPERIMENT  
WIND TUNNEL

SIZE: 11 IN. x 11 IN.  
SPEED: 64 FT/SEC

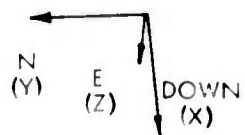


Figure 2. Photograph of Wind Tunnel Installation

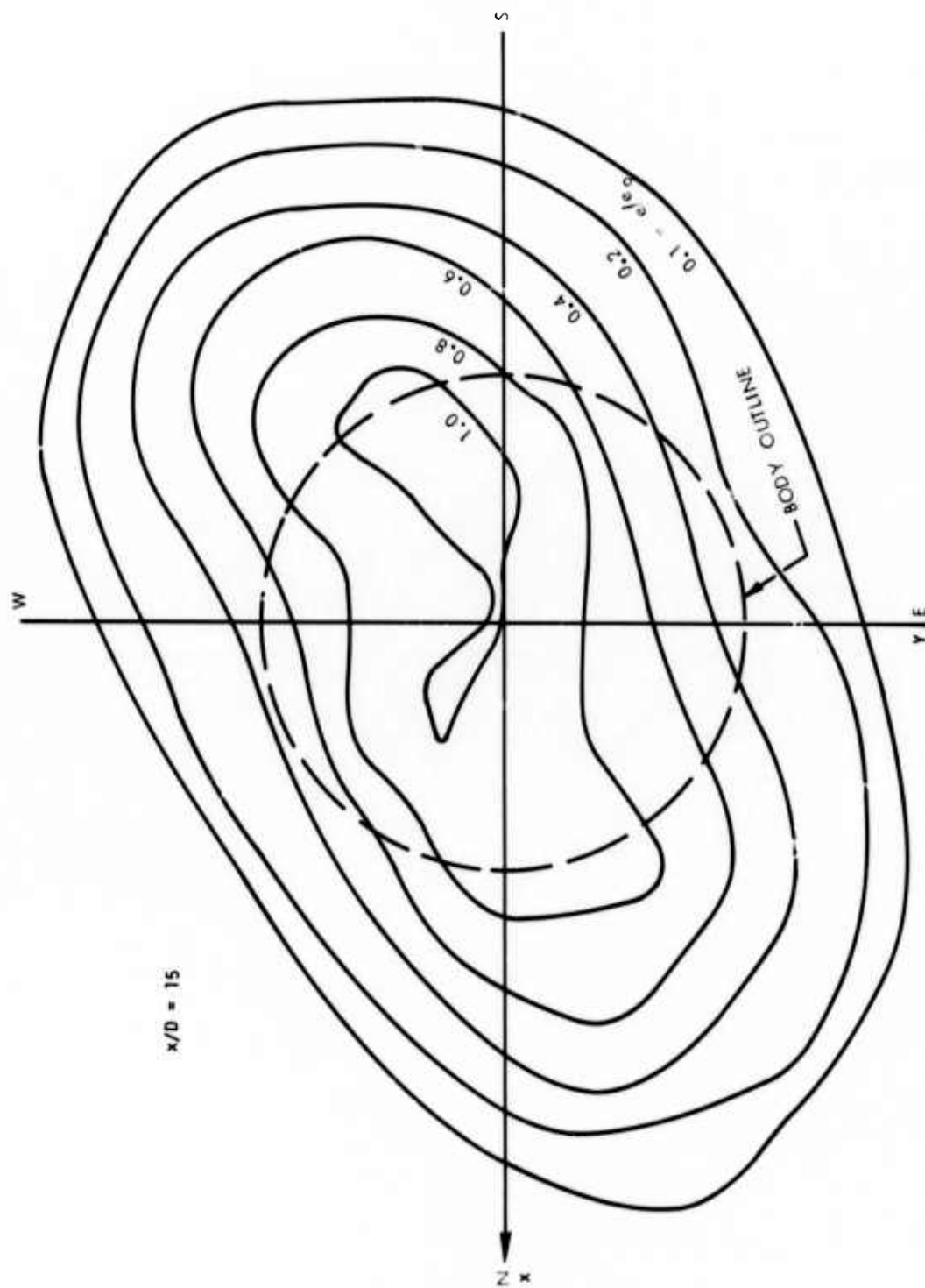


Figure 3. Example of Observed Wake Asymmetry



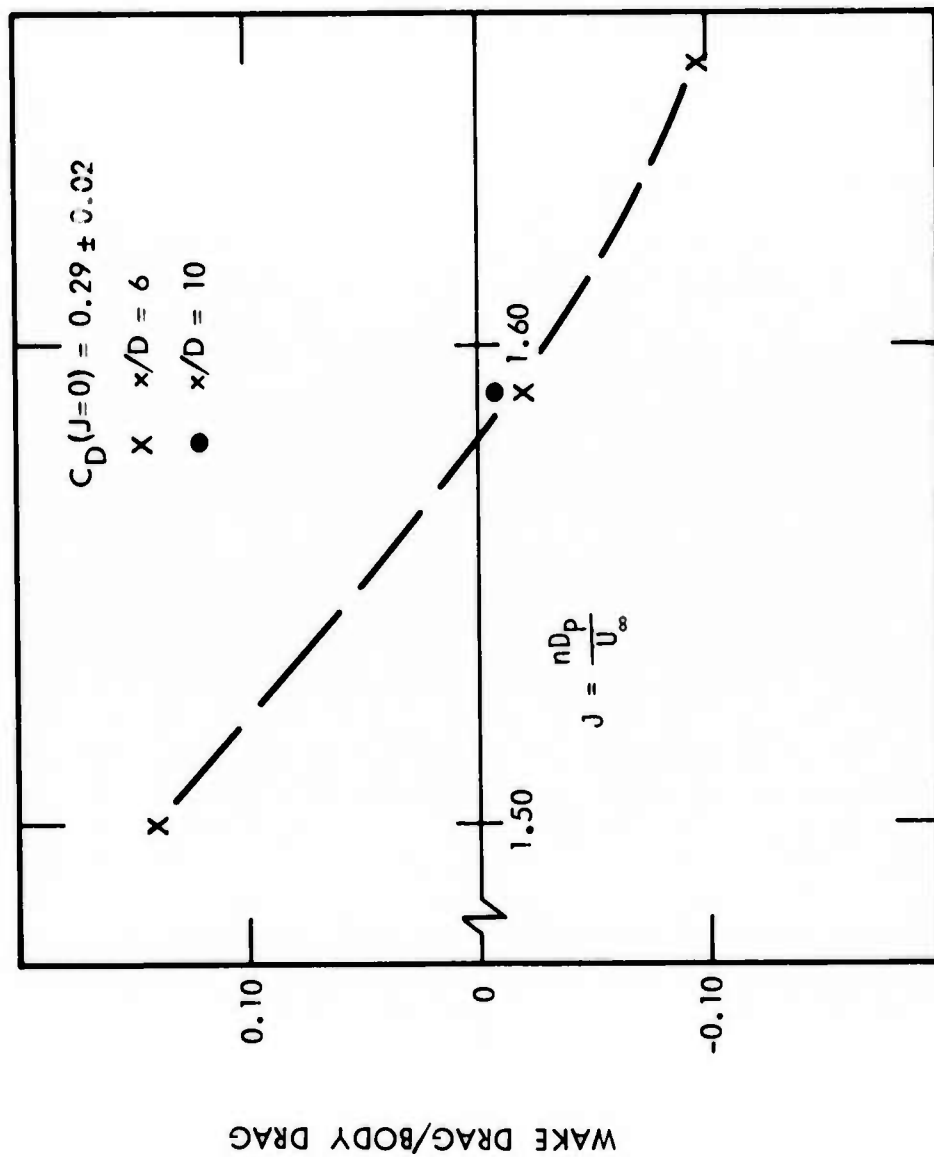


Figure 4. Evaluation of Propeller Speed for Thrust = Drag

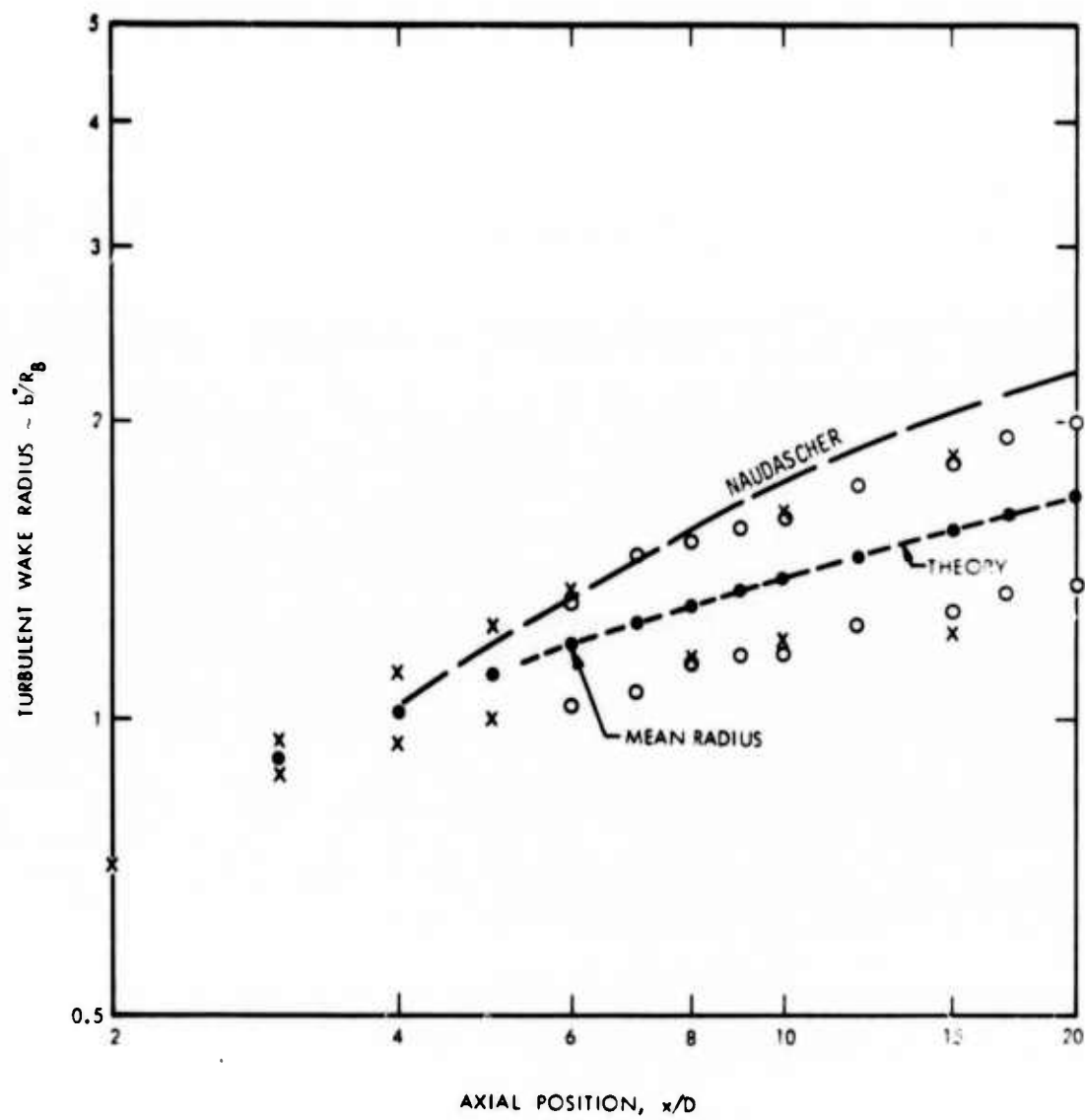


Figure 5. The Turbulent Wake Radius

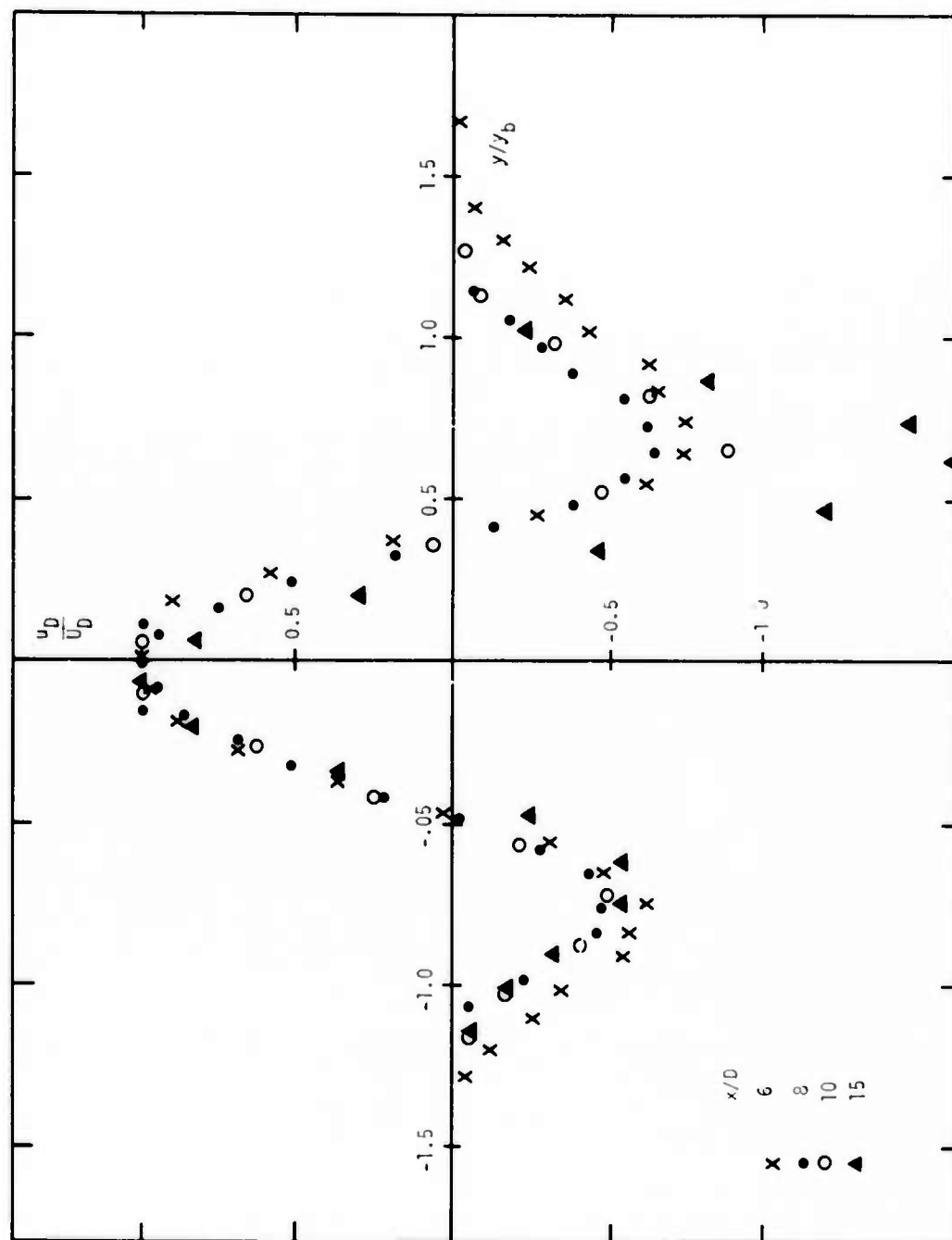


Figure 6. Axial Velocity Profiles,  $x/D > 6$

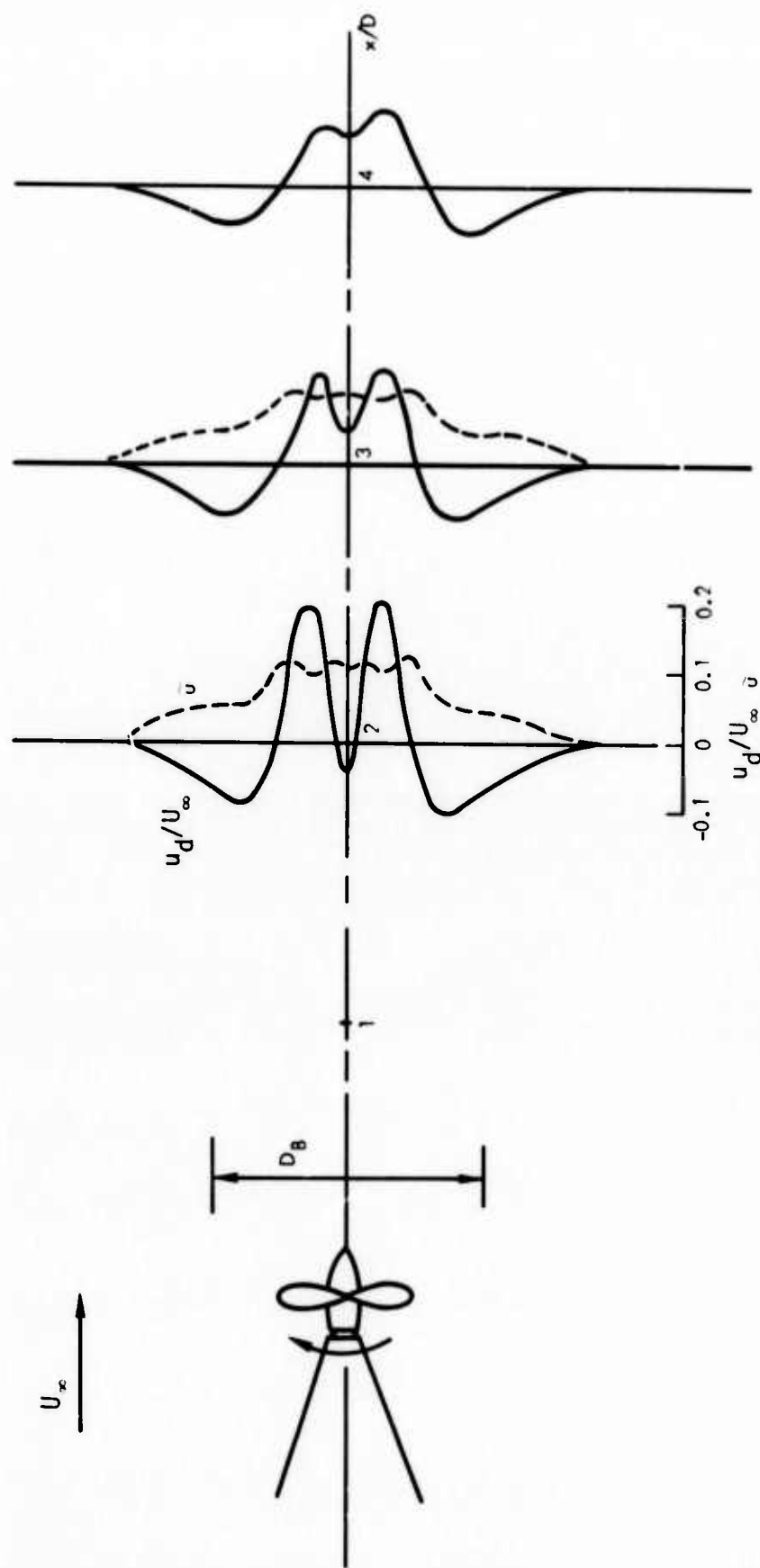


Figure 7. Axial Velocity and Turbulence Profiles for  $2 \leq x/D \leq 4$

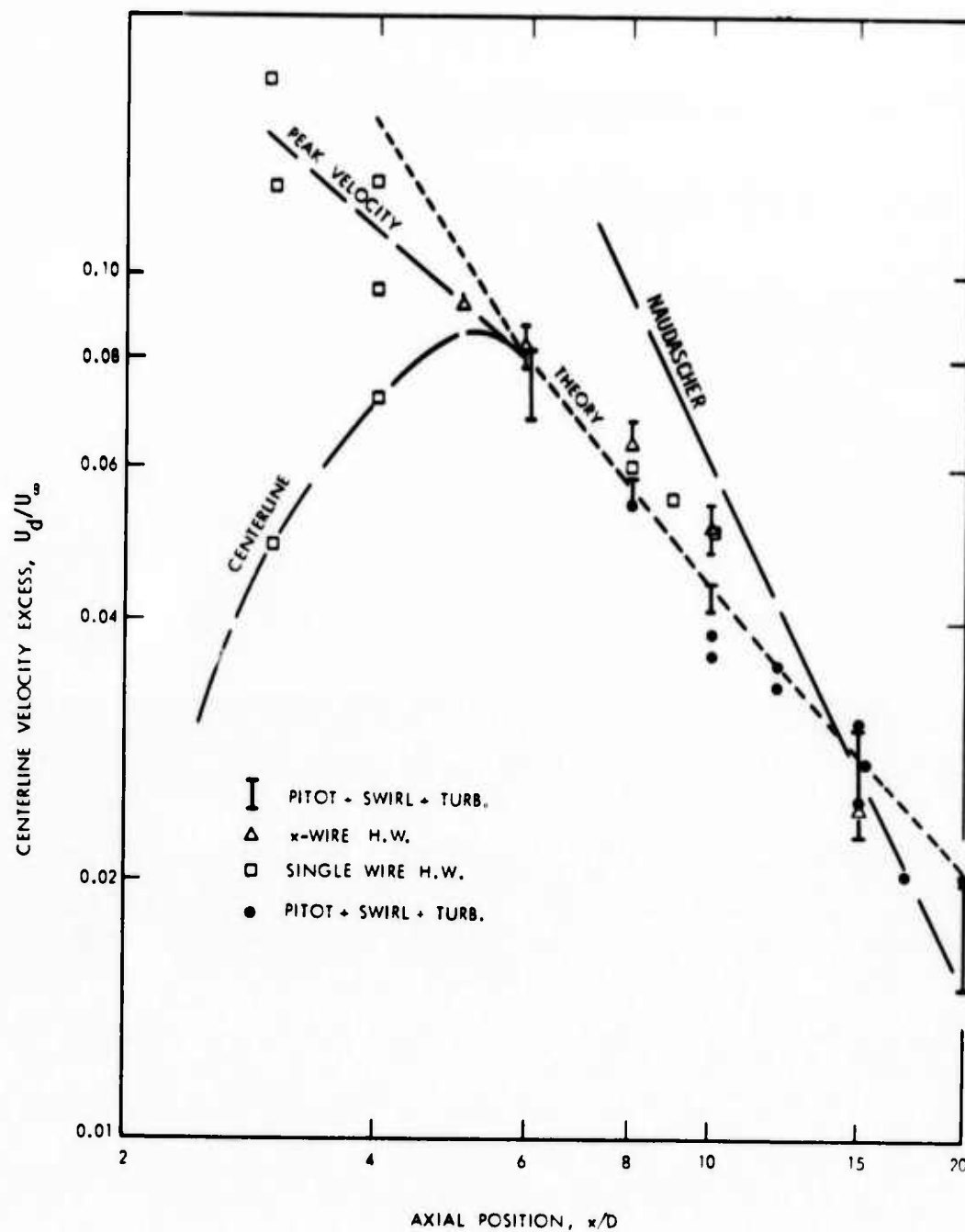


Figure 8. The Decay of the Centerline Velocity Excess

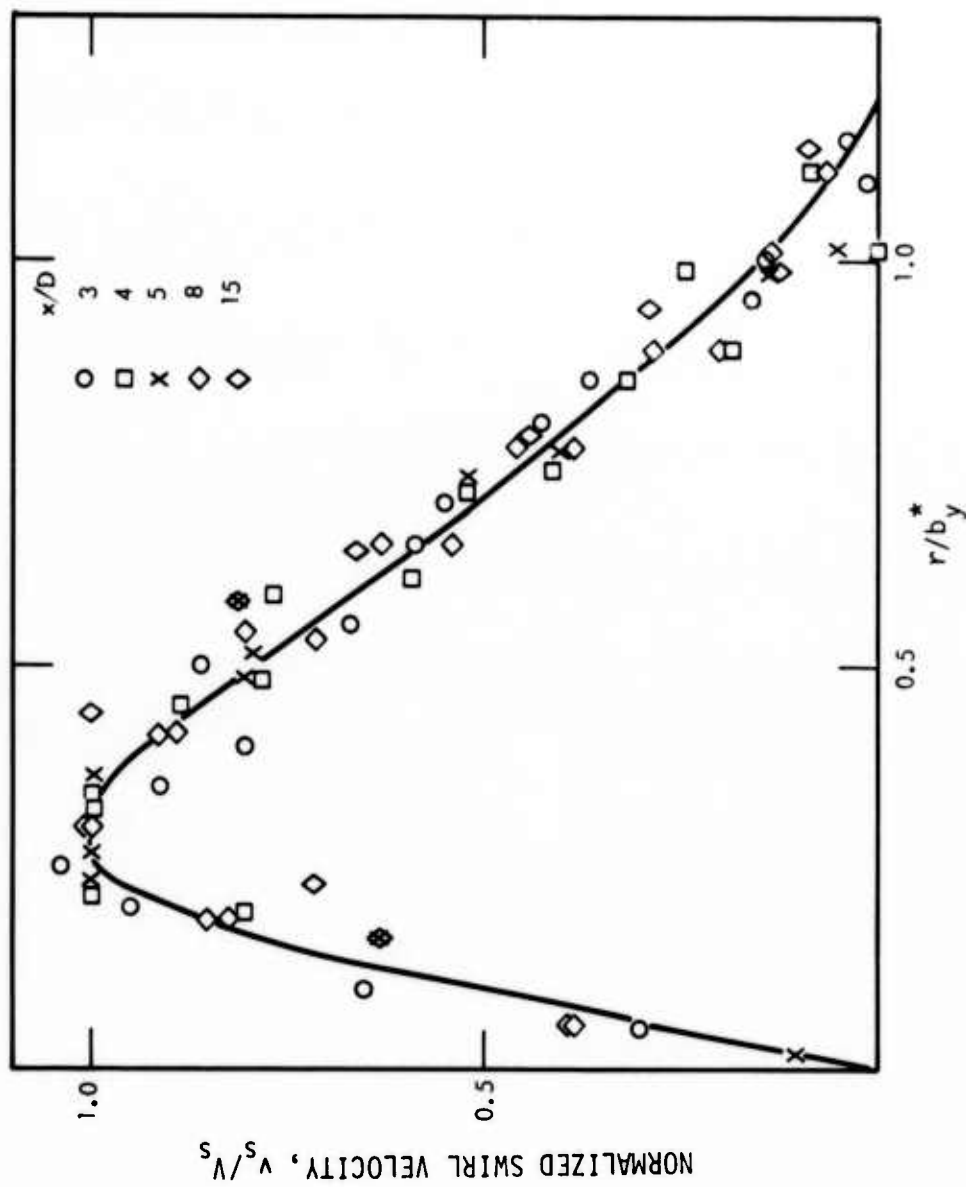


Figure 9. Swirl Velocity Radial Profiles

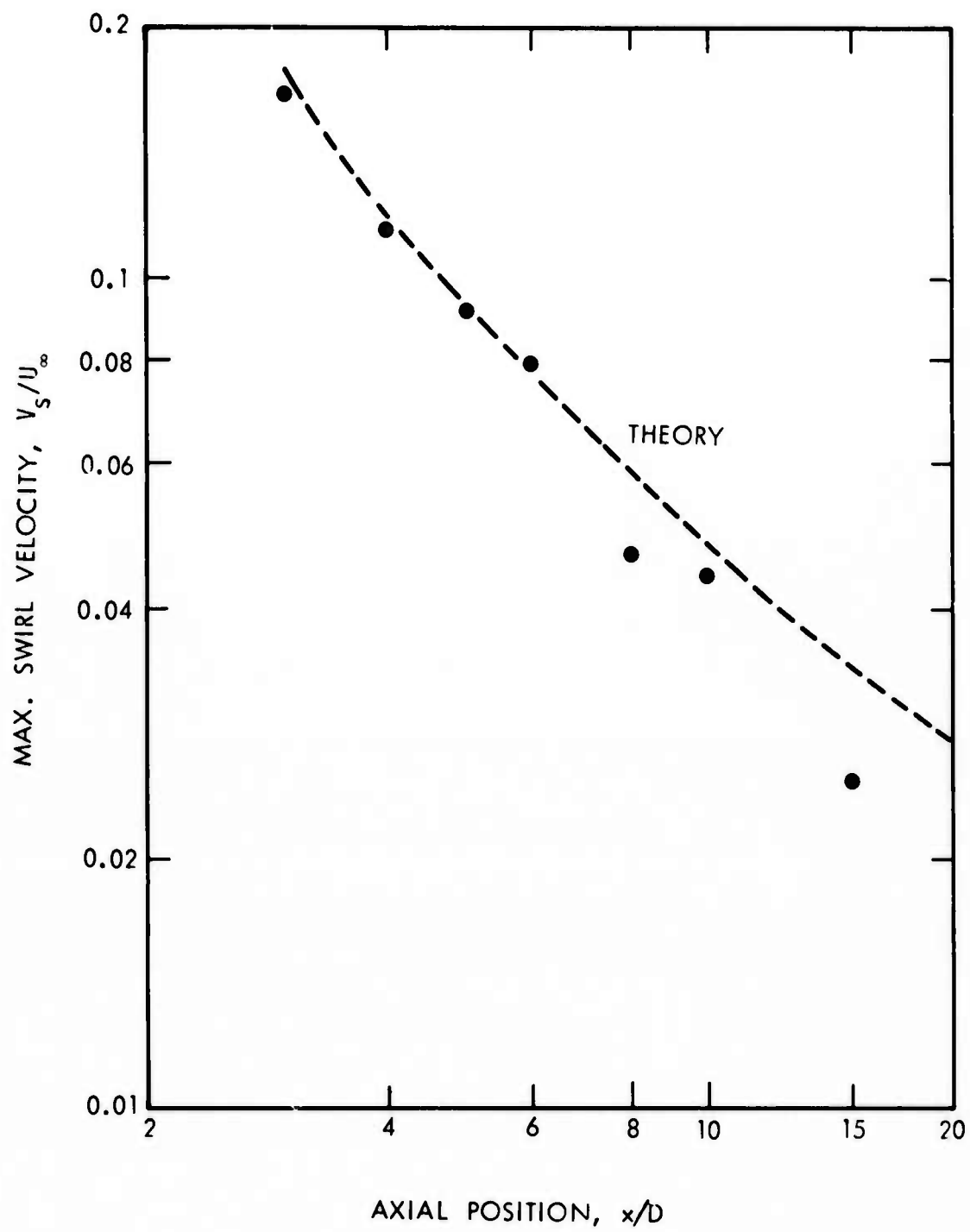


Figure 10. The Decay of the Maximum Swirl Velocity



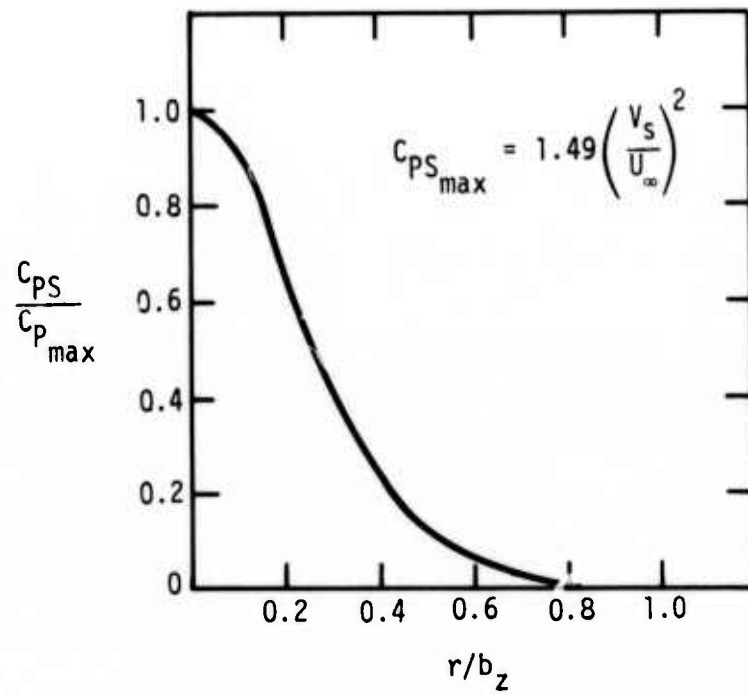


Figure 11. The Swirl-Induced Radial Pressure Distribution

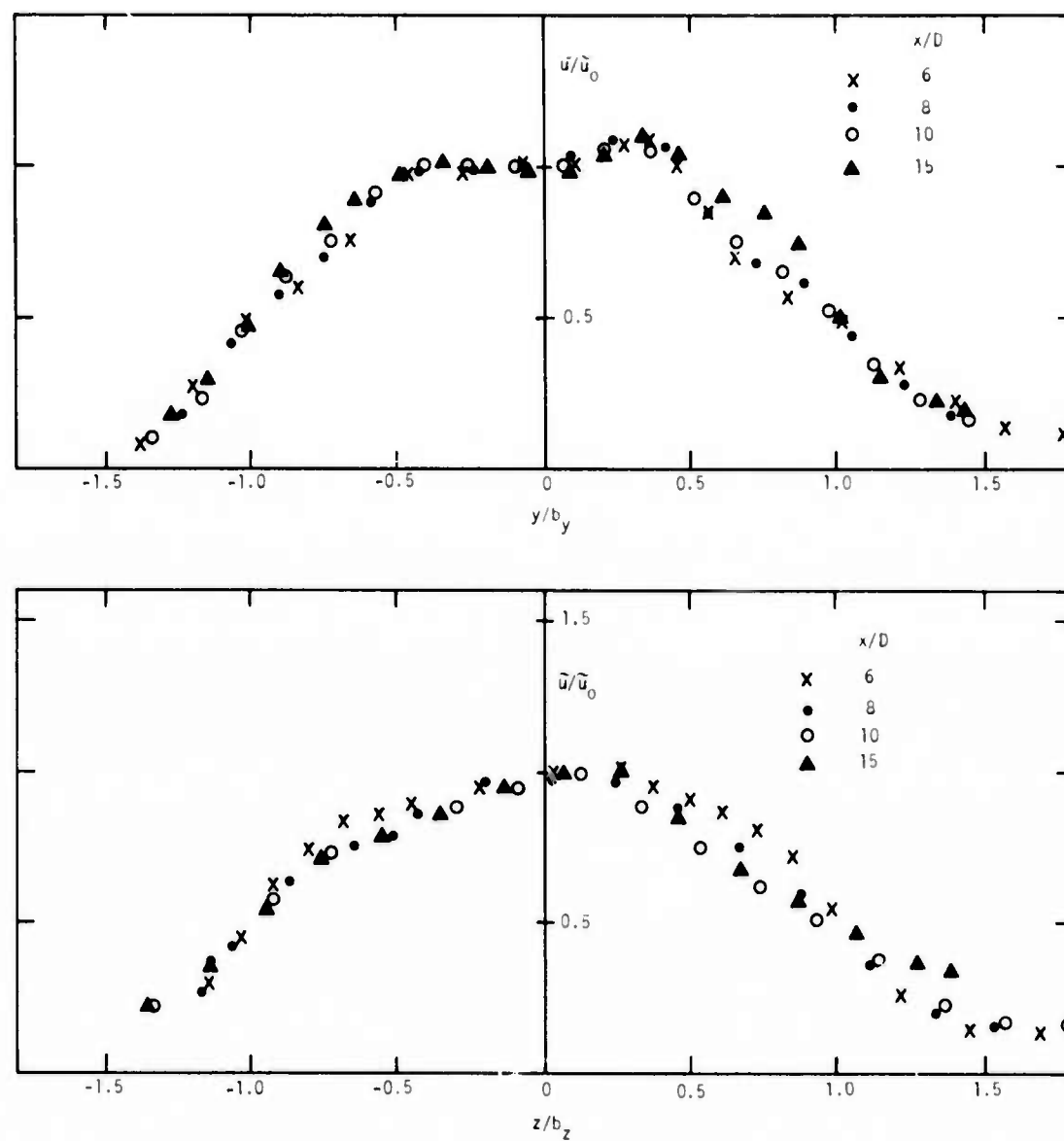


Figure 12. Profiles of Axial Turbulent Intensity

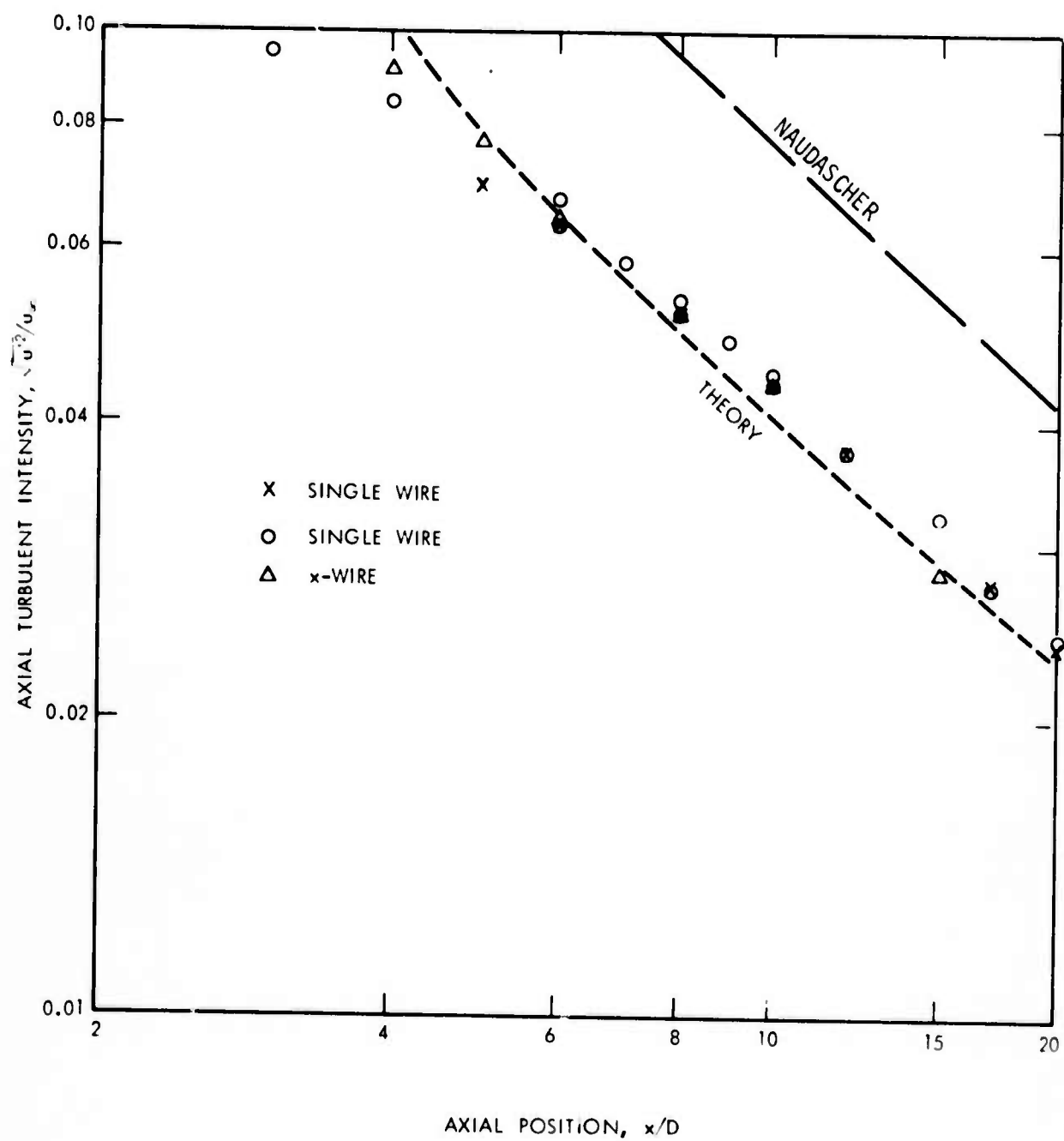


Figure 13. The Decay of the Turbulent Intensity

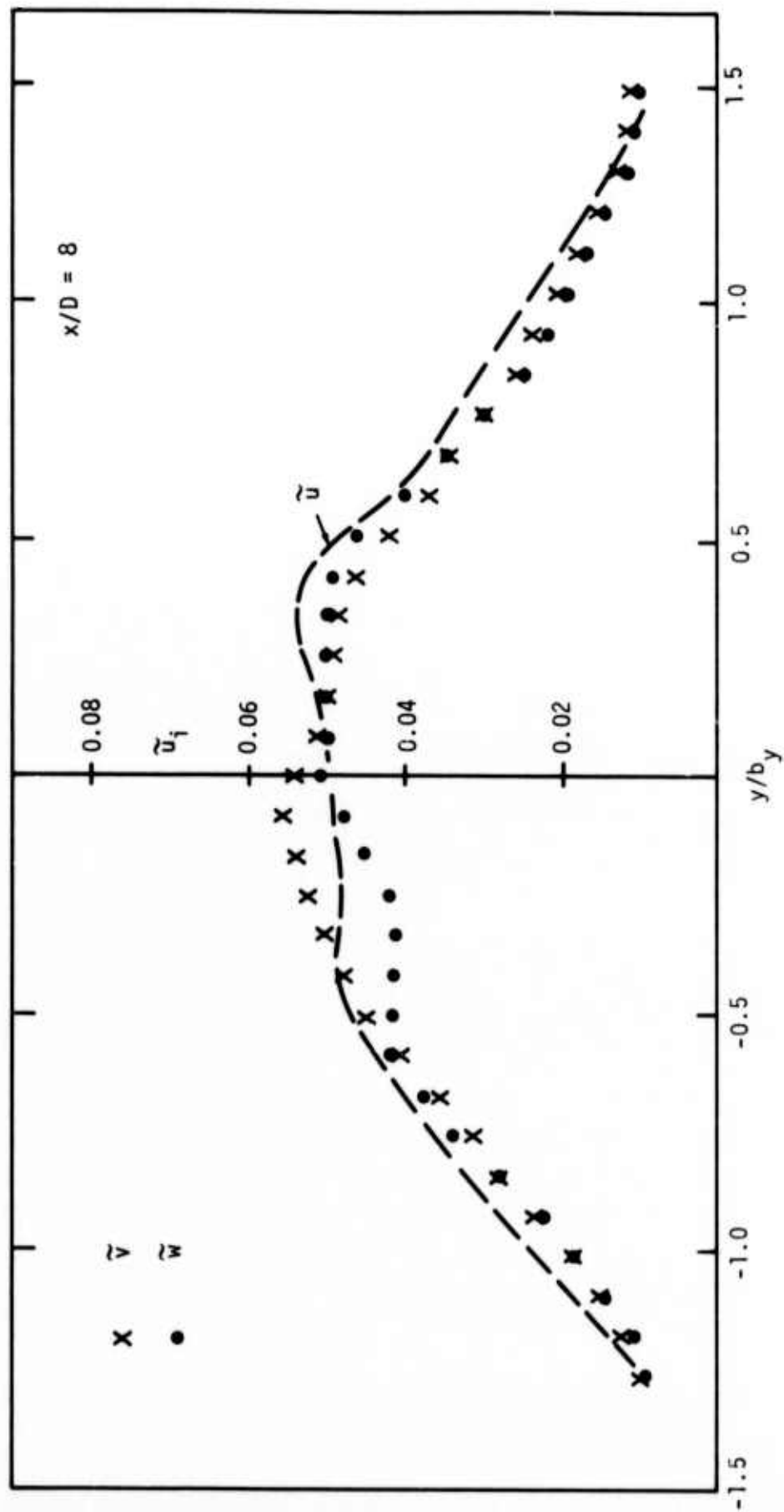


Figure 14. Transverse Turbulence Profiles

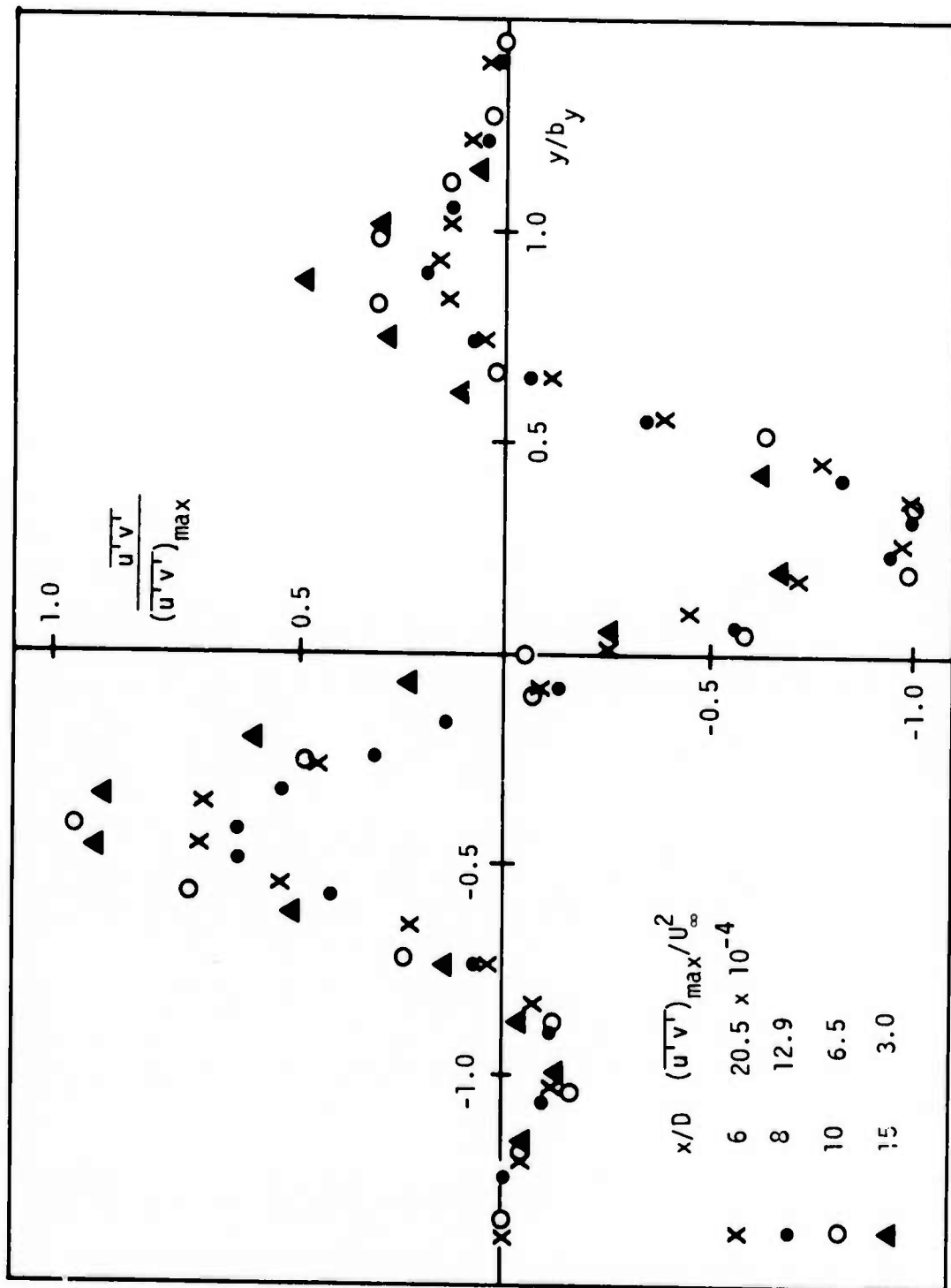


Figure 15. Reynolds Stress Profiles

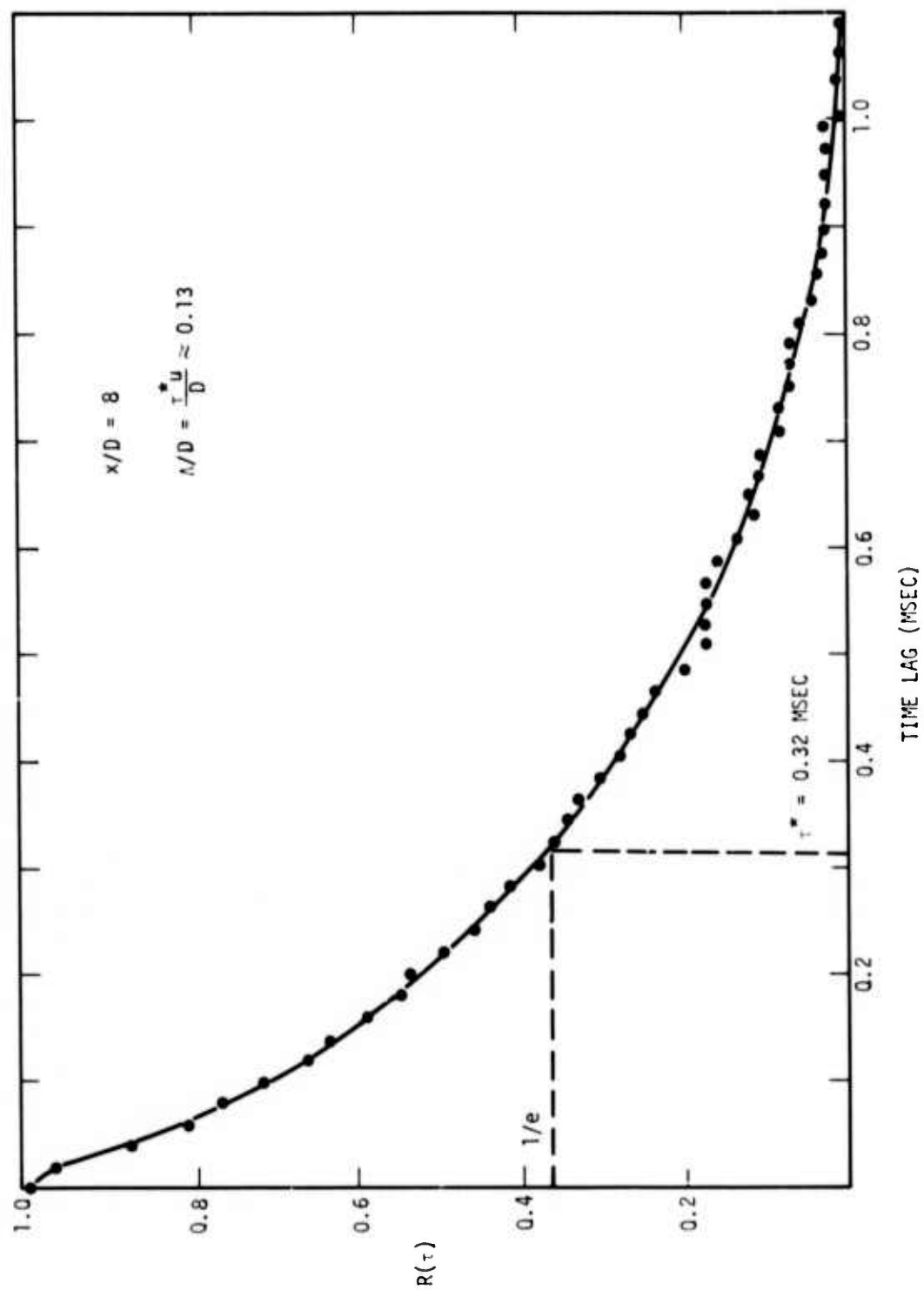


Figure 16. Example of Autocorrelation Function of  $u'$

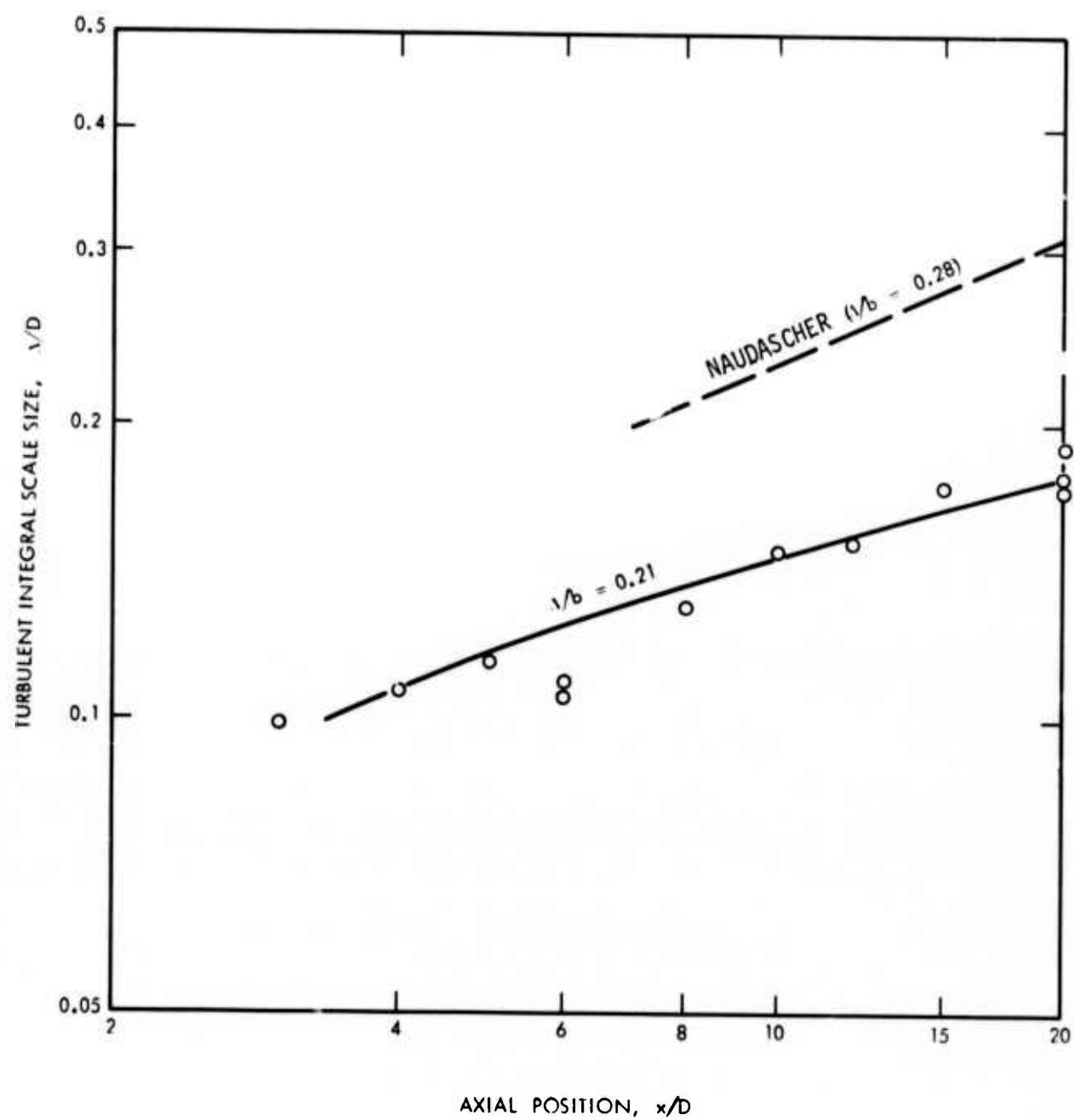


Figure 17. Integral Scale of Turbulence on the Wake Axis



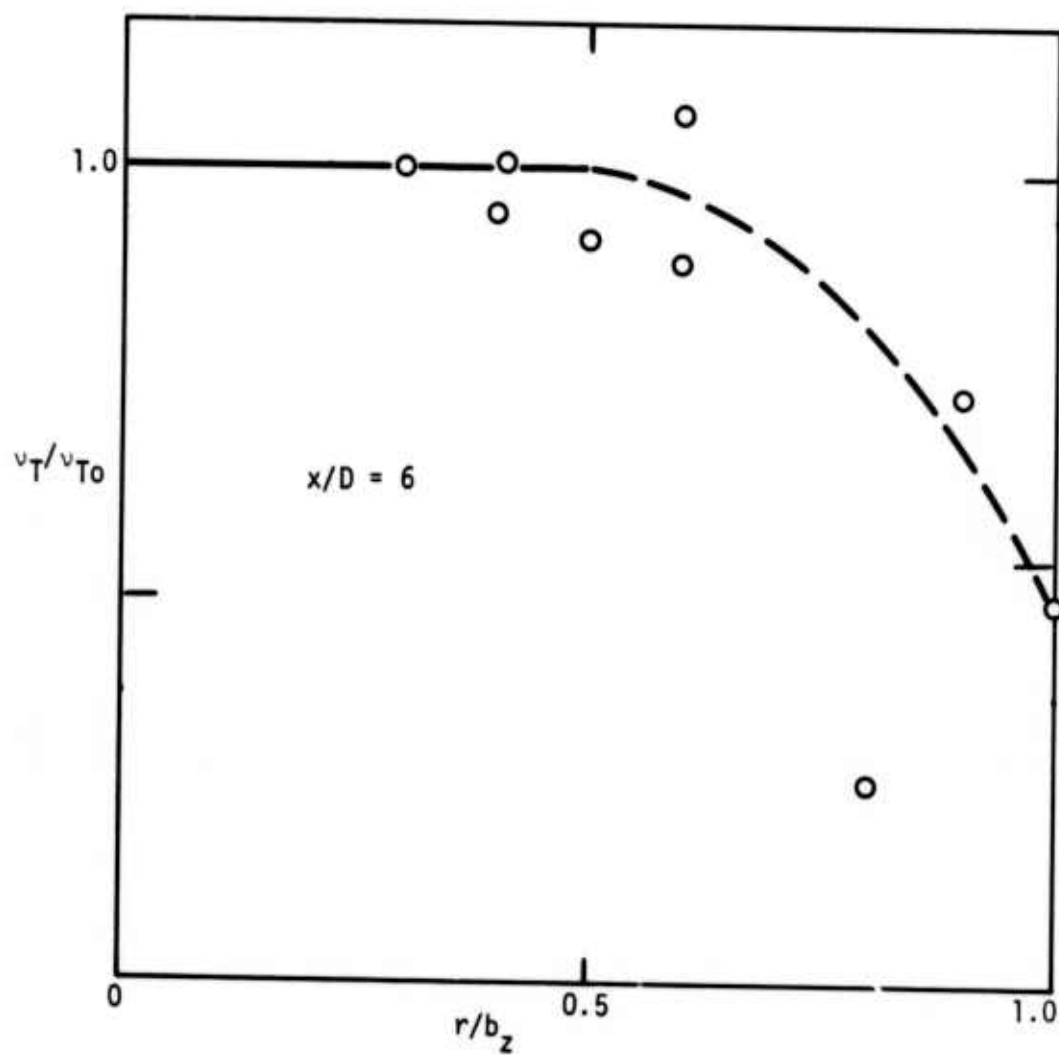


Figure 18. Radial Variation of Eddy Viscosity

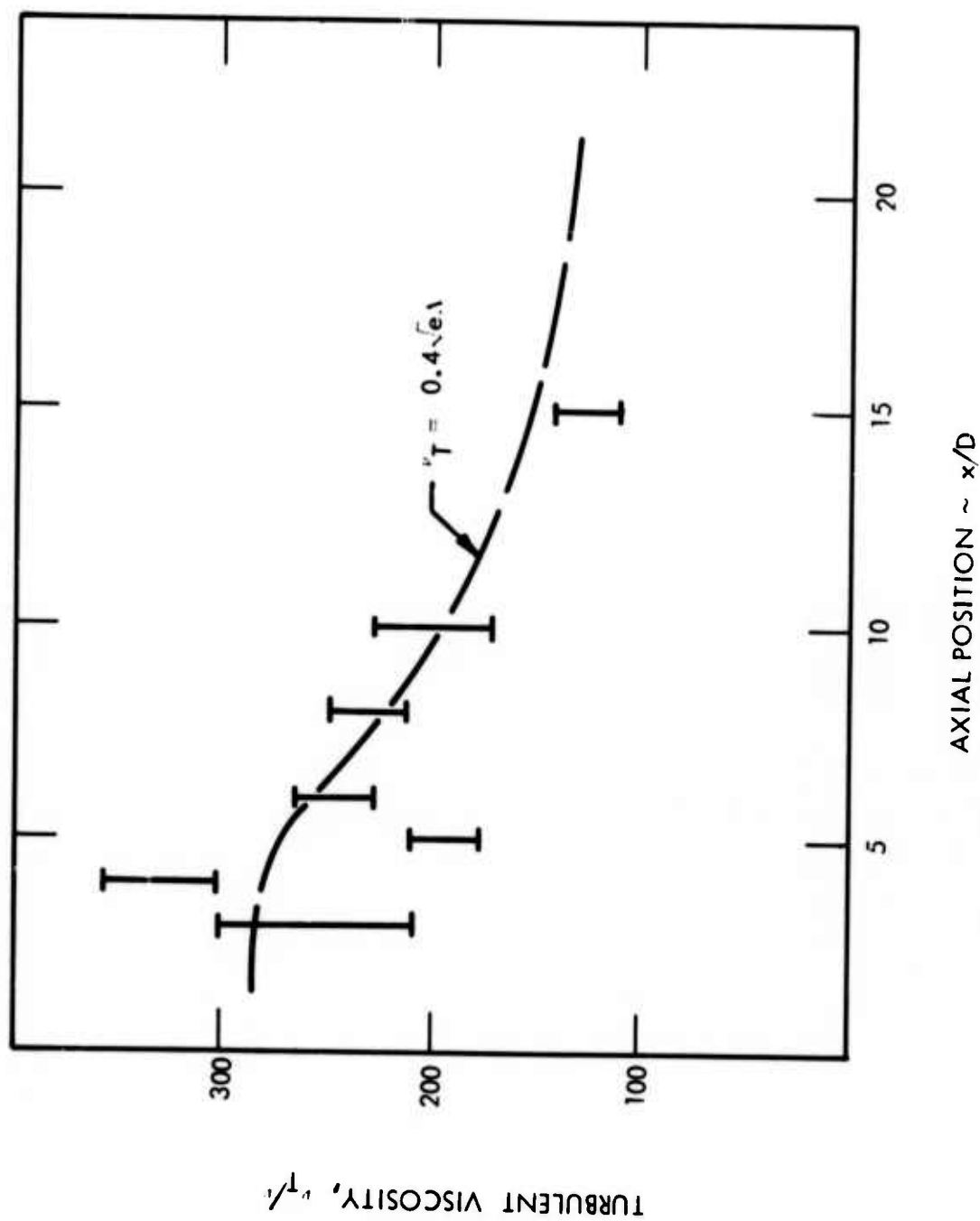


Figure 19. Axial Variation of Eddy Viscosity

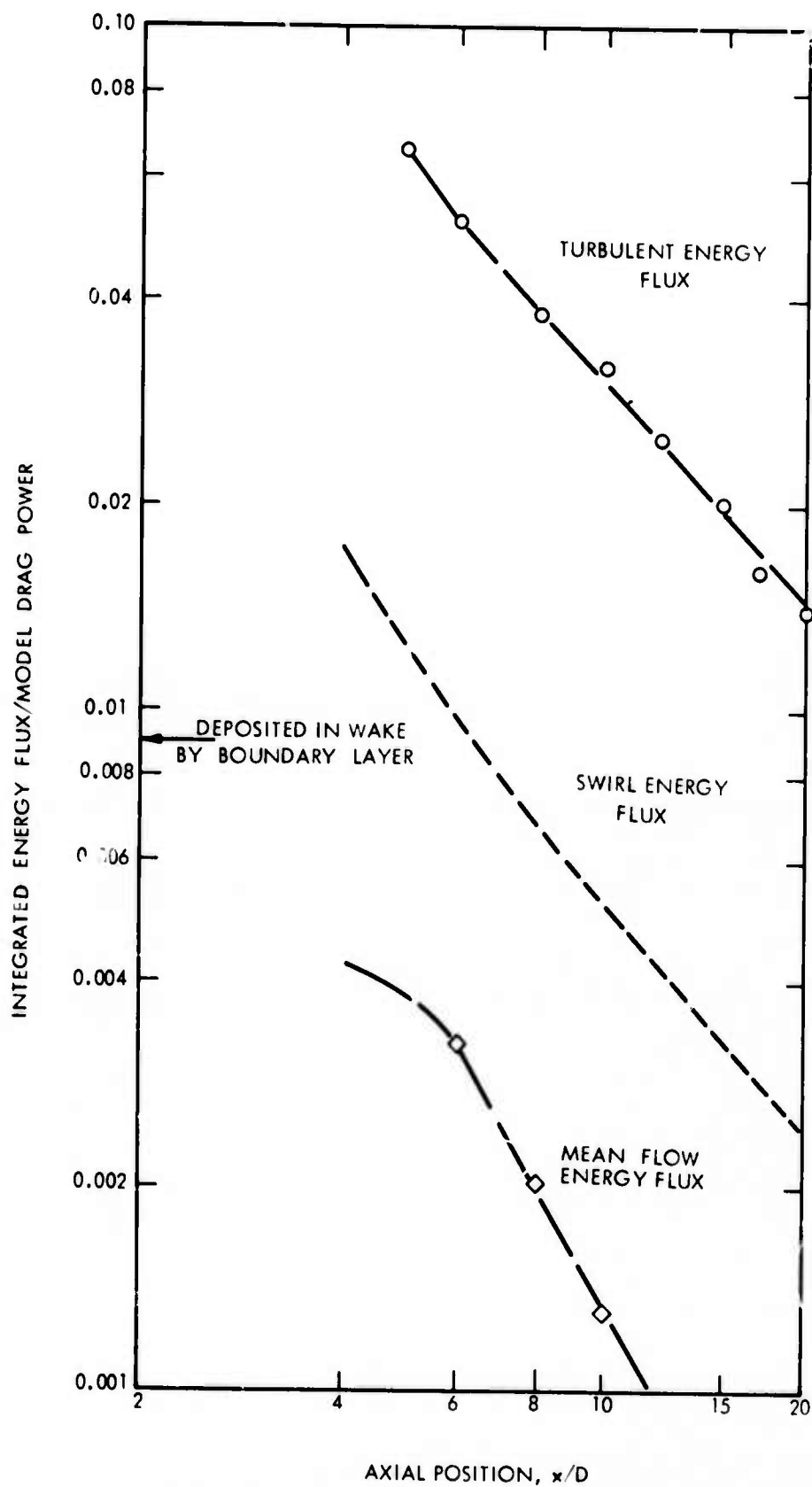


Figure 20. Energy Flux Measurements in the Momentumless Wake